

Statistical Analysis of Convective Updrafts in Tropical Cyclone Rainbands Observed by Airborne Doppler Radar

Nicholas R. Barron¹ , Anthony C. Didlake Jr.¹ , and Paul D. Reasor²

¹Department of Meteorology and Atmospheric Science, The Pennsylvania State University, University Park, PA, USA,

²Hurricane Research Division, NOAA/Atlantic Oceanographic and Meteorological Laboratory, Miami, FL, USA

Key Points:

- Updrafts in tropical cyclone rainbands reach their greatest size, strength, and frequency in the downshear half of the storm
- The convective-scale secondary circulation patterns of these updrafts are mainly influenced by the large-scale shear and updraft altitude
- The in-up-out convective-scale circulation pattern in rainbands is the most frequent and has the deepest updrafts and reflectivity towers

Correspondence to:

A. C. Didlake,
didlake@psu.edu

Citation:

Barron, N. R., Didlake, A. C. Jr., & Reasor, P. D. (2022). Statistical analysis of convective updrafts in tropical cyclone rainbands observed by airborne Doppler radar. *Journal of Geophysical Research: Atmospheres*, 127, e2021JD035718. <https://doi.org/10.1029/2021JD035718>

Received 17 AUG 2021

Accepted 6 MAR 2022

Abstract Ten years of airborne Doppler radar observations are used to study convective updrafts' kinematic and reflectivity structures in tropical cyclone (TC) rainbands. An automated algorithm is developed to identify the strongest rainband updrafts across 12 hurricane-strength TCs. The selected updrafts are then collectively analyzed by their frequency, radius, azimuthal location (relative to the 200–850 hPa environmental wind shear), structural characteristics, and secondary circulation (radial/vertical) flow pattern. Rainband updrafts become deeper and stronger with increasing radius. A wavenumber-1 asymmetry arises, showing that in the downshear (upshear) quadrants of the TC, updrafts are more (less) frequent and deeper (shallower). In the downshear quadrants, updrafts primarily have in-up-out or in-up-in secondary circulation patterns. The in-up-out circulation is the most frequent pattern and has the deepest updraft and reflectivity tower. Upshear, the updrafts generally have out-up-in or in-up-in patterns. The radial flow of the updraft circulations largely follows the vortex-scale radial flow shear-induced asymmetry, being increased low-level inflow (outflow) and midlevel outflow (inflow) in the downshear (upshear) quadrants. It is hypothesized that the convective-scale circulations are significantly influenced by the vortex-scale radial flow at the updraft base and top altitudes. Other processes of the convective life cycle, such as bottom-up decay of aging convective updrafts due to increased low-level downdrafts, can influence the base altitude and, thus, the base radial flow of the updraft circulation. The findings presented in this study support previous literature regarding convective-scale patterns of organized rainband convection in a mature, sheared TC.

1. Introduction

Spiral rainbands are ubiquitous features in tropical cyclones (TCs) that constitute much of the area and total precipitation of the overall TC. TC rainbands contain convective and stratiform features that can involve complex interactions with the boundary layer (e.g., Barnes et al., 1983; Bu et al., 2017; C. K. Yu & Chen, 2011; Didlake & Houze, 2009; Kepert, 2018; Riemer et al., 2010), eyewall (e.g., Y. Chen & Yau, 2001; Wang, 2002), and surrounding environment (e.g., Dai et al., 2019; Riemer & Montgomery, 2011; Willoughby et al., 1984). These interactions could lead to significant impacts on TC evolution. Rainbands can act as a local source of potential vorticity (PV) that spirals into the PV central core, which can help strengthen the storm (Franklin et al., 2006; May & Holland, 1999). Oppositely, storm weakening can occur when rainband downdrafts, induced either by precipitation forcing or compensating subsidence, reduce the θ_e of boundary layer air feeding into the eyewall (e.g., Alland et al., 2021a, 2021b; Barnes et al., 1983; C. K. Yu & Chen, 2011; Li & Dai, 2020; Li & Wang, 2012a; Powell, 1990a, 1990b; Sawada & Iwasaki, 2010a, 2010b). Diabatic heating within the strong rainband convection can also produce a local pressure minimum due to hydrostatic adjustment, which reduces the radial flow into the eyewall and possibly weakens the TC (Powell, 1990a; Wang, 2009). Rainbands can also alter the TC structure through processes such as accelerating the local tangential winds and expanding the TC wind field (e.g., Didlake & Houze, 2013b; Hill & Lackmann, 2009; Rozoff et al., 2012; Smith et al., 2009) or contributing to the development of a secondary eyewall outside of the pre-existing primary eyewall (e.g., Bell et al., 2012; C. L. Yu et al., 2021; Didlake et al., 2018; Qiu & Tan, 2013; Willoughby et al., 1982). In order to fully understand the overall role of rainbands in TC evolution, we must understand the different rainband structures and processes that can occur in nature. The current study addresses this gap in knowledge by exploring the detailed structure of the observed rainband convection.

Rainbands can exist in a wide variety of manners, with differing spatial structures and temporal evolutions at all stages of a TC's lifetime. Despite such variety, rainbands often exhibit repeated location, composition, and behavior patterns due to large-scale environmental factors. One such factor is the vertical, deep-layer (200–850 hPa)

environmental wind shear. In the presence of sufficient deep-layer wind shear, TC rainbands are organized into a broad, asymmetric complex termed the Stationary Band Complex (SBC; Willoughby et al., 1984). Right of the deep-layer shear vector, the SBC exhibits discrete or connected convective cells that grow and mature as they propagate downwind (Hence & Houze, 2012a). These cells generally exhibit low-level radial inflow that turns upward into intense buoyant updrafts, then turns radially outward in the mid-troposphere (5–8 km; Barnes et al., 1983; Hence & Houze, 2008; Powell, 1990a, 1990b; Samsury & Zipser, 1995). This flow pattern can build local tangential wind jets through stretching and tilting of the background vorticity field. The convective cells also contain two distinct downdrafts: a low-level downdraft originating at 2–4 km altitude driven by precipitation drag and an inner-edge downdraft originating at 6–8 km altitude formed along the inner boundary of the rainband (Didlake & Houze, 2009). Traveling downwind into the left-of-shear half of the TC, the rainband convection weakens and collapses into a broad, homogeneous band of predominantly stratiform precipitation. In this downwind stratiform rainband, Didlake and Houze (2013b) and Didlake et al. (2018) found mesoscale descending radial inflow that was forced by midlevel latent cooling and extended into the boundary layer. Modeling studies show that this mesoscale downdraft forms a cold pool that can trigger and maintain new convective updrafts embedded in the larger stratiform band (C. L. Yu & Didlake, 2019; C. L. Yu et al., 2021; Li & Dai, 2020).

Rainband convection also varies with radius from the storm center due to the radially changing influences of the vortex circulation and the surrounding environment. Convective updrafts at smaller radii generally have a shallower vertical extent than those farther from the storm center (Didlake & Houze, 2013a; Hence & Houze, 2012a; Li & Wang, 2012a). This effect may be due to decreasing convective available potential energy for buoyant updrafts at smaller radii (Bogner et al., 2000; Li & Fang, 2019; Molinari et al., 2012) or rapid filamentation and dissipation of convective elements in inner core regions of strong horizontal wind shear (Rozoff et al., 2006). Distant rainbands, located far from the storm center, are buoyancy-driven convective elements that propagate outward like squall lines with a locally generated cold pool (Moon & Nolan, 2015; Tang et al., 2014). Just outside the eyewall of a mature TC, rainbands often behave as convectively coupled vortex-Rossby waves that propagate along the radial vorticity gradient of a TC vortex (e.g., Corbosiero et al., 2006; Fischer et al., 2020; Guimond et al., 2020; Li & Wang, 2012a; Li et al., 2017; Montgomery & Kallenbach, 1997; Wang, 2002).

Many previously mentioned observational and modeling studies involve case examinations of one or a small number of storms (e.g., Barnes & Stossmeister, 1986; Barnes et al., 1991; Didlake & Houze, 2013a, 2013b; Moon & Nolan, 2015; Tang et al., 2014, 2018). Unfortunately, such case studies do not individually capture the full variety of rainband features that occur in nature. In contrast, other studies may examine the inner core structures (i.e., the eyewall and rainbands immediately outside of the eyewall) in a large number of TCs (e.g., Reasor et al., 2013). However, these studies usually use azimuthally averaged profiles to analyze behaviors within the rainband, which potentially obscure smaller-scale rainband features important for examining the full TC evolution. Some TC studies do capture the details of convective-scale features across multiple TC cases. Jorgensen et al. (1985) used flight level observations to examine the vertical velocities in four mature hurricanes, characterizing their magnitudes and spatial distributions in the eyewall and rainband regions. Black et al. (1996) extended this characterization of vertical motions across seven hurricanes using tail Doppler radar vertical incidence observations. With this expanded dataset, they described the vertical structures and reflectivity features associated with these drafts. Wadler et al. (2018) tracked individual convective bursts that initiated near the eyewall in multiple observed storms, and they determined the frequency, location, and burst characterizations that were most important for rapid intensification of the TC. Using ground-based radar observations, C. K. Yu et al. (2018) found that TC outer rainbands were more likely to develop squall-line-like characteristics. Terwey and Rozoff (2014) developed an automated updraft tracking algorithm specifically for use with numerical simulations and applied it successfully to two different models; they found notable differences between the models in updraft frequency, structure, and evolution. Li and Fang (2019) also used model simulations to study the buoyancy of convective updrafts and found that the updraft buoyancy is significantly larger in the downshear half of the TCs. These studies successfully track and examine some aspects of individual convective updrafts. The current study seeks to extend the prior work by using a similar tracking methodology in an observation-based analysis of a large number of rainband structures analyzing a wider scope of updraft features.

This study analyzes the convective-scale structures of TC rainbands captured by 10 years' worth of airborne Doppler radar observations from Atlantic and central Pacific basin hurricanes. In particular, we focus on convective rainband updrafts and their associated convective-scale kinematic and reflectivity structures. We first

identify the strongest rainband updrafts in each storm and then statistically analyze their specific characteristics, including their frequency, radial location, shear-relative location, depth, strength, and secondary circulation flow pattern. The result is an improved understanding of the variety of observed rainband updraft structures across a variety of hurricane-strength TCs. An overview of the observational data and methods is presented in Section 2. In Sections 3 and 4, we investigate how updraft size and location vary with radius and shear-relative azimuth. In Section 5, the secondary circulation around each updraft is investigated. This section includes an analysis of shear-relative quadrant composites, and the development and application of an objective updraft circulation classification algorithm. The conclusions for this study are in Section 6.

2. Data and Methods

2.1. Airborne Radar Observations

The airborne observations used for this study were obtained by the National Oceanic and Atmospheric Administration (NOAA) WP-3D (P3) Tail Doppler radar (TDR). The P3 TDR are vertically scanning X-band (3.22 cm) Doppler radars, dual transmitting since 2017, and have beams oriented approximately 20° fore and aft. The fore and aft Doppler-wind measurements, collected as the aircraft traverses the TC, are used to retrieve the three-dimensional wind field out to the maximum unambiguous range of ~50 km from the radar (Lorsolo et al., 2013). The data for this study are from 59 missions across 12 hurricane-strength ($\geq 33 \text{ ms}^{-1}$) TCs in the Atlantic and central Pacific basins, spanning from 2010 to 2019 (see Table 1 for a comprehensive list). The TC maximum wind speeds are taken from the NOAA National Hurricane Center HURDAT2 dataset (Landsea & Franklin, 2013), providing wind speeds at 6-hr intervals during the lifetime of each TC. These intensities are then interpolated to the middle time of each mission. Most missions performed nominal survey patterns that consisted of multiple radial passes through the eyewall while optimizing the azimuthal coverage of the storm.

The radar observations were first analyzed with an automated quality control and dealiasing algorithm successfully applied in other studies using TDR data (e.g., Fischer et al., 2020; Rogers et al., 2012; Reasor et al., 2013). 3D velocity vectors were then retrieved using a variational technique that constrains and optimizes the radar projection equation along with mass continuity and boundary conditions (Gamache, 1997; Gao et al., 1999; Reasor et al., 2009). The retrieval then maps the reflectivity and velocity fields onto a Cartesian grid with a horizontal spacing of 2 km and vertical spacing of 0.5 km. Storm vortex centers were determined using a real-time analysis of flight level data (Willoughby & Chelmon, 1982). The average storm motion for each mission was subtracted from the wind retrievals to obtain the storm-relative velocity field in all subsequent analyses. These data were then interpolated to a storm-centered cylindrical coordinate system with a grid spacing of $2 \text{ km} \times 2^\circ \times 0.5 \text{ km}$ in the radial, azimuthal, and vertical directions. Finally, to account for varying storm sizes, the radial coordinate of each updraft is normalized by the radius of maximum wind, here defined as the azimuthally averaged 2 km tangential wind maximum for each mission.

2.2. Updraft Selection and Updraft Properties

Using the retrieved velocity fields for each radial pass, the following procedure selected individual convective rainband updrafts. First, vertical velocity thresholds were defined for each mission by analyzing the distribution of all vertical velocities in a given mission at 2 km altitude and at radii larger than $1.5r^*$, where r^* is the radius of maximum wind. The average r^* is approximately 45 km, and the first and third quartiles of the r^* distribution are 25 and 50 km radius, respectively. The threshold for a given mission was set at the 95th percentile of the vertical velocity distribution (see Table 1 for values). We used this percentile method to account for inherent variability across all missions. Next, convective updrafts were defined by clustering all connected data pixels where the vertical velocity was greater than the vertical velocity threshold; this process forms a 3D boundary around each updraft element. The number and size of the selected updraft elements were sensitive to this threshold value; the chosen combination of 2 km altitude and 95th percentile for the initial distribution analysis yielded threshold magnitudes that best captured the naturally occurring number and size of the selected updraft elements, based on our subjective analysis. To prevent the inclusion of problematic updraft elements (i.e., updrafts suspected to have notable errors in the retrieval solution), selected updrafts must also pass several other tests. Geometrically, updraft elements must include at least two horizontal grid points or four vertical grid points (i.e., at least 2 km in either direction). To evaluate and refine the convective nature of selected updrafts, we applied a convective-stratiform

Table 1
Storm Name and Aircraft Mission ID for the Tail Doppler Radar Data Used in This Study

Storm: Mission ID	# Passes	# Updrafts	Shear magnitude (ms ⁻¹)	Shear direction °	Maximum winds (ms ⁻¹)	Threshold (ms ⁻¹)
EARL: 100829I1	4	43	2.4	146.7	42.6	1.14
EARL: 100830H1	3	40	6.6	26.4	54.4	0.89
EARL: 100830I1	3	28	5.7	243.9	59.2	1.49
EARL: 100901H1	2	34	6.7	47.3	56.4	0.9
EARL: 100901I1	2	36	10.6	55.9	62.0	1.35
EARL: 100902H1 ^a	3	36	10.1	34.1	60.1	1.13
ARTHUR: 140703I1	1	10	10.4	54.2	42.2	1.22
EDOUARD: 140914I1	3	9	6.6	45.6	37.8	1.12
EDOUARD: 140915H1	2	19	8.5	94.9	48.5	1.13
EDOUARD: 140915I1	2	14	7.7	89.3	48.3	1.21
EDOUARD: 140916H1 ^a	2	16	8.8	86.2	50.8	0.99
EDOUARD: 140916I1	2	1	9.6	83.0	47.7	1.37
EDOUARD: 140917H1	2	4	13.1	53.2	41.2	1.01
GONZALO: 141016I1	2	2	7.3	356.2	64.0	1.37
GONZALO: 141017I1 ^a	2	1	7.2	54.6	56.5	1.37
MATTHEW: 160930I1	2	20	16.8	19.0	60.3	0.84
MATTHEW: 161001I1 ^a	2	5	13.7	31.3	67.1	1.02
MATTHEW: 161005I1	3	1	10.7	319.9	54.4	0.76
MATTHEW: 161005I2	3	12	7.8	345.6	54.0	0.71
MATTHEW: 161006I2 ^a	5	89	9.1	12.8	60.0	0.85
MATTHEW: 161007I1	1	20	7.8	37.4	51.2	1.34
HARVEY: 170824H2	3	35	1.9	58.5	36.4	0.57
HARVEY: 170825H1	3	29	11.0	329.7	45.6	0.61
HARVEY: 170825H2	2	18	5.7	32.3	53.7	0.8
IRMA: 170903H1	3	18	3.3	179.1	51.4	0.62
IRMA: 170904H1 ^a	4	59	6.3	165.6	56.2	0.76
IRMA: 170904H2	3	16	4.2	219.3	63.5	0.8
IRMA: 170905H1	3	25	4.6	341.9	75.9	0.81
IRMA: 170905H2	4	34	3.0	234.5	79.7	0.76
IRMA: 170908H1 ^a	4	12	8.3	178.8	69.6	0.58
IRMA: 170908H2	3	8	4.8	112.2	73.9	0.47
MARIA: 170922H1	3	10	16.0	36.2	55.4	1.05
MARIA: 170923H1 ^a	3	9	12.3	243.0	51.4	0.89
MARIA: 170924H1	4	34	11.4	19.6	48.9	0.58
NATE: 171007H1	4	19	4.2	340.6	40.3	0.68
LANE: 180820H1 ^b	3	24	10.6	18.9	56.5	0.68
LANE: 180820H2 ^b	3	21	10.7	21.8	59.0	0.77
LANE: 180821H1 ^b	4	29	9.7	26.1	66.3	0.56
LANE: 180822H1 ^b	3	39	6.3	50.6	71.8	0.52
FLORENCE: 180909H1	3	37	11.2	15.9	34.9	0.59
FLORENCE: 180910H1	4	27	7.6	183.9	60.4	0.61
MICHAEL: 181008H1	3	21	14.0	0.2	43.5	0.67
MICHAEL: 181009H1	5	45	13.3	200.1	46.5	0.6

Table 1
Continued

Storm: Mission ID	# Passes	# Updrafts	Shear magnitude (ms ⁻¹)	Shear direction °	Maximum winds (ms ⁻¹)	Threshold (ms ⁻¹)
MICHAEL: 181009H2	5	44	11.6	331.7	57.1	0.55
MICHAEL: 181010H1	3	28	9	316.3	64.1	0.69
DORIAN: 190828H1	3	14	5.7	300.0	38.1	0.57
DORIAN: 190829H1	4	48	7.3	302.2	38.6	0.87
DORIAN: 190829H2	3	38	5.1	290.0	42.0	0.81
DORIAN: 190830H1	4	30	6.9	303.2	49.6	0.9
DORIAN: 190830H2	3	43	5.6	320.9	58.9	0.82
DORIAN: 190831H1	5	43	7.7	318.7	64.7	0.87
DORIAN: 190831H2	4	31	7.9	346.9	70.1	0.8
DORIAN: 190901H1	3	30	9.8	341.0	81.1	0.56
DORIAN: 190902H2	5	37	7.0	347.0	59.8	0.98
DORIAN: 190903H1	5	30	6.6	314.4	51.8	0.73
DORIAN: 190904H1	6	25	8.9	71.1	51.0	0.62
DORIAN: 190905H1	8	13	7.3	99.0	51.0	0.74
DORIAN: 190905H2	8	15	10.3	35.3	46.5	0.57

Note. Given for each mission are the number of eyewall passes made, the number of convective updrafts selected, 200–850 hPa wind shear magnitude and direction (meteorological azimuth of vector arrow), maximum wind speed of the TC, and vertical velocity threshold for updraft selection. The naming format for the missions are YYMMDDAN, where “YY” is the year, “MM” is the month, “DD” is the day of the month, “A” is the aircraft, and “N” is the mission number for that aircraft on a given day. Unless noted otherwise, all missions are from Atlantic basin storms.

^aMissions have a mature secondary eyewall. ^bMissions from storms in the central Pacific basin.

classification algorithm on the reflectivity field (see Didlake & Houze, 2009; Steiner et al., 1995) and determined the fraction of the vertical-velocity-defined updraft element that is convectively classified. Only updrafts with 40% or more convectively classified pixels are included in the analysis. We found this value to produce an optimal balance of maximizing updraft quantities while also reducing the inclusion of stratiform-dominated updrafts. Figure 1 shows an example of selected updraft elements in Hurricane Matthew overlaid on 2-km-altitude vertical velocity and reflectivity fields. The radial, azimuthal, and vertical locations of each updraft element are defined by the vertical-velocity-weighted centroid. The updraft outlines show the horizontal extent of the updraft slice at 2 km altitude.

To exclude the eyewall and distant rainbands from our analysis, only updrafts positioned greater than $2r^*$ and less than $9r^*$ are included. Azimuthal locations are measured relative to the pointing directions of two vectors: the storm motion vector and the deep-layer environment shear vector, each with azimuth increasing clockwise. The storm motion vector is calculated by measuring the differential distance between the Hurricane Research Division’s Best Track dataset for vortex center positions every 20 min. The zonal and meridional components of the track velocity are then smoothed via a Lanczos filter to eliminate small-scale perturbations in the TC’s motion. The resulting velocity vector determines the direction and magnitude of the track motion. These velocities are then interpolated to the time of each eyewall pass. The deep-layer (200–850 hPa) environmental wind shear vector is calculated from the National Center for Environmental Prediction Reanalysis-2 dataset (see Kanamitsu et al., 2002) using the vortex-removal procedure detailed in Davis et al. (2008). In this procedure, the irrotational and nondivergent components of the wind are subtracted from the 200 and 850 hPa horizontal wind fields. The remaining background flow is averaged over a disk extending out to 800 km from the storm center to produce two vectors; the 850 hPa vector is then subtracted from the 200 hPa vector to yield the shear vector.

In storms where a secondary eyewall is present, we aimed to count only updrafts in rainbands and not those in mature secondary eyewalls. Our approach first defines a “mature” secondary eyewall as any local maximum in the 0.5–2 km layer average axisymmetric tangential wind that has a corresponding quadrant local maximum in at least three shear-relative quadrants. If one is identified, the selected updrafts must be radially outside the mature secondary eyewall. In this manner, we still include observations of storms with a secondary eyewall.

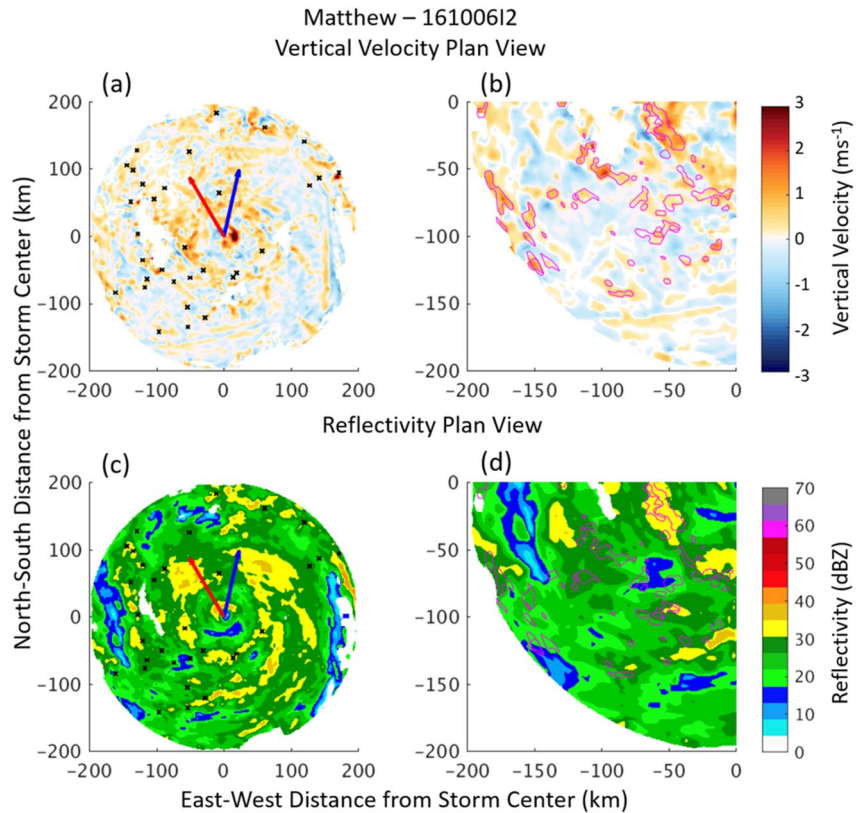


Figure 1. Plan view showing convective updraft locations overlaid on (a), (b) vertical velocity and (c), (d) reflectivity at 2 km altitude from Hurricane Matthew on 06 October 2016 (mission 16100612). At this time, Matthew had maximum winds of 61 ms^{-1} . Shown in (a) and (c) are full plan views with black crosses denoting convective updraft horizontal locations. Blue and red arrows are the environmental shear and storm track vectors, respectively. Shown in (b) and (d) are plan views zoomed in on the southwest quadrant with convective updraft horizontal extent outlined in magenta.

The normalized radius (r^*), shear-relative azimuth (θ_s), and track-relative azimuth (θ_t) describe the location of each updraft. Additional characteristics for each updraft are the updraft base and top altitude, depth, and strength. The updraft base and top describe the lowermost and uppermost altitudinal positions of an updraft element. Updraft depth is the difference between the top and base altitudes. Lastly, the updraft strength is defined as the maximum vertical velocity within the updraft.

3. Updraft Size, Strength, and Location in an Axisymmetric Framework

This section analyzes the distributions of the updraft characteristics with respect to the normalized radius; this analysis essentially collapses the statistics into an axisymmetric framework. Figure 2 shows the joint frequency distributions of updraft normalized radius versus updraft base altitude, top altitude, depth, and strength.

Overall, the frequency of updrafts decreases with increasing radius, as shown by the single-dimension frequency distribution (see Figure 2). Since the typical P3 flight pattern is optimized to observe the inner core, the ratio of observed area to annulus area is lower at larger radii. This likely contributes to this frequency decrease. In Figure 2a, the updraft base altitude does not change appreciably with radius. The base altitude shows two modes at 1–2 km and 0–1 km base altitude at $2-4r^*$ and $4-6r^*$, respectively. A peaked distribution of base altitude is present at $2-4r^*$, and then, the distribution flattens at larger radii. Beyond $6r^*$, the updraft counts decrease significantly. Given the low updraft counts, we do not discuss the updraft characteristics at these radii. In Figure 2b, the updraft top altitudes are largely above 6 km altitude and have distributions that change in structure with radius. Between 2 and $5r^*$, the top altitudes have a wide distribution with modes shifting from 6–8 km to 8–10 km at $4r^*$. At $5-6r^*$, a bimodal distribution emerges, with local frequency maxima at 6–8 km and 10–12 km. The updraft depths in Figure 2c show a slight trend of deeper updrafts with the increasing radius. At smaller radii ($2-4r^*$),

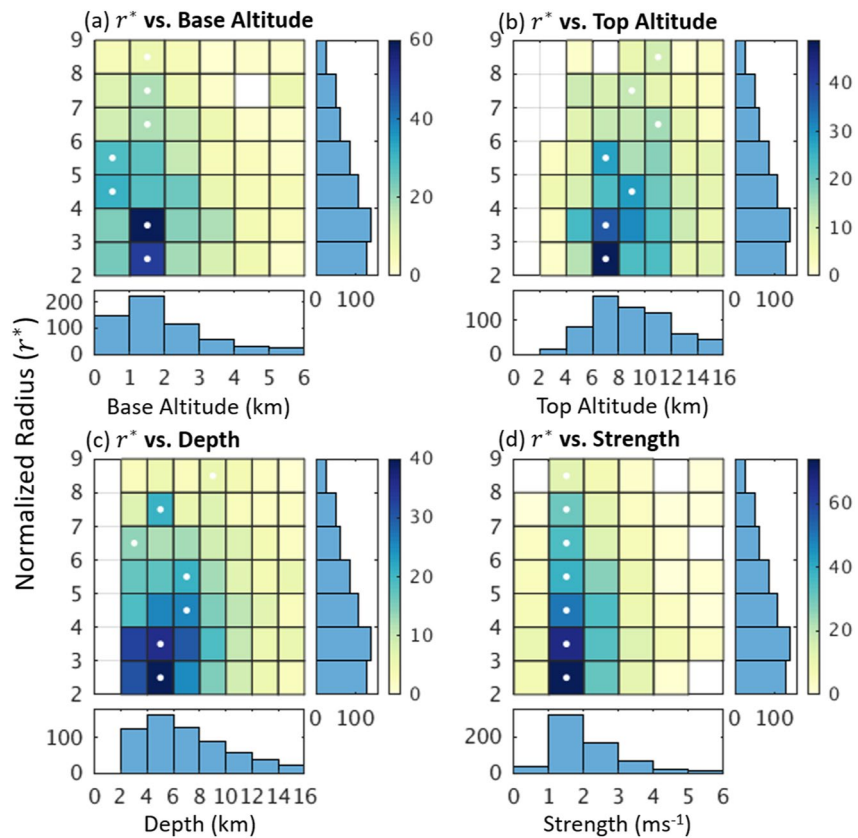


Figure 2. Bivariate histograms of updraft normalized radius (r^*) versus (a) updraft base altitude, (b) updraft top altitude, (c) updraft depth, and (d) updraft strength. Along each axis are the single-dimension histograms for each variable. The colorbar shows frequency counts. White dots indicate the mode of the distribution within each ordinate bin.

the mode is between 4 and 6 km, and the distribution has a broad tail with a notable number of updrafts growing as deep as 12 km. Between 4 and $6r^*$, the depth mode increases to 6–8 km. Figure 2d shows that the updraft strength is often between 1 and 2 ms^{-1} . Between 4 and $6r^*$, the 1–2 ms^{-1} and 2–3 ms^{-1} updrafts occur at similar frequencies, unlike those updrafts at smaller radii. The aforementioned shift in the velocity distribution indicates that the updrafts at larger radii are more likely to be stronger than those at smaller radii, which is consistent with our finding of increasing depth with radius.

These findings have some consistency with previous observations of TC rainbands. Didlake and Houze (2013a) showed that, in a single case study, rainband convective updrafts at larger radii had greater depths, vertical velocity magnitudes, and tops than those at smaller radii. Our results reflect these same findings (within 2– $6r^*$) across many storms. The primary reason for these convective radial variations is likely a general increase in convective available potential energy (CAPE) with a larger radius (Bogner et al., 2000; Molinari et al., 2012). Hence and Houze (2012a) examined reflectivity observations across many storms from the Tropical Rainfall Measuring Mission Precipitation Radar and found that outer rainband convection had higher altitude reflectivity peaks than those of inner rainband convection, consistent with the current updraft observations.

4. Updraft Size, Strength, and Location in an Asymmetric Framework

We now analyze the updraft frequencies and characteristics with respect to their azimuthal location; this analysis will highlight asymmetric variations in convective rainband patterns. Figure 3a shows the joint frequency distribution of updraft's normalized radius versus shear-relative azimuthal angle. The single-dimension shear-relative angle histogram shows that updrafts more frequently occur downshear with a slight tendency toward the downshear-left (DL) quadrant; this finding agrees with previous observations and modeling studies (Hence &

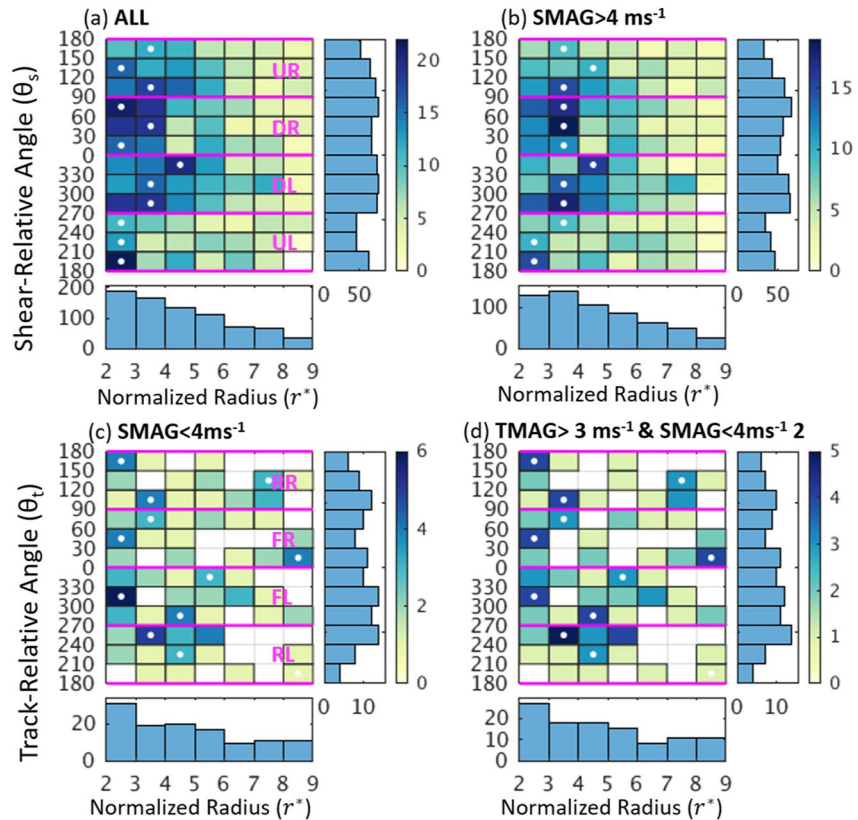


Figure 3. Bivariate histograms of (a), (b) updraft shear-relative angle ($^\circ$) versus r^* and (c), (d) updraft track-relative angle ($^\circ$) versus r^* . Panel (a) includes data from all missions. Missions with shear magnitudes (SMAG) $> 4 \text{ ms}^{-1}$ are in (b). Missions with SMAG $< 4 \text{ ms}^{-1}$ are in (c). Missions with both storm track magnitudes (TMAG) $> 3 \text{ ms}^{-1}$ and SMAG $< 4 \text{ ms}^{-1}$ are in (d). Single dimension histograms and ordinate distribution modes (white dots) are shown. Pink horizontal lines denote the shear-relative quadrants [upshear-right (UR), downshear-right (DR), downshear-left (DL), and upshear-left (UL)] or track-relative quadrants (rear-right, front-right, front-left, rear-left).

Houze, 2012a; Li & Wang, 2012b). In the left-of-shear storm half, the modes appear in a pattern that moves radially inward, which may indicate a spiral convective rainband repeated across many storms.

Previous studies have shown that a shear-organized rainband complex generally occurs with moderate or strong ($\geq 5 \text{ ms}^{-1}$) deep-layer environmental shear vector (e.g., Corbosiero & Molinari, 2002; Hence & Houze, 2012b; Rogers et al., 2003; Wingo & Cecil, 2010). To account for this, Figure 3b only includes updrafts within storms that have a shear magnitude of at least 4 ms^{-1} during the observation period. Using a 4 ms^{-1} threshold reduces the total number of updrafts from Figure 3a by 13%. While 5 ms^{-1} has been used as the threshold for weak to moderate shear in many previous studies, we chose to use 4 ms^{-1} instead to include more elements from our dataset; we did not find a notable pattern difference between selecting 4 or 5 ms^{-1} that affects our overall conclusions.

In Figure 3b, the left-of-shear half exhibits the same inward moving modal pattern as in Figure 3a; this updraft spiral is consistently prominent at stronger shear values. One notable difference in Figure 3b is the more prominent frequency peaks of downshear updrafts. The emergence of a clearer frequency peak in the DR is consistent with previous studies that found more active rainband convection in this quadrant (Corbosiero & Molinari, 2002, 2003; Didlake & Houze, 2013a). Also, the right-of-shear storm half exhibits a steadier mode at $3\text{--}4r^*$ than that in Figure 3a. Overall, applying the shear magnitude threshold introduced some additional organization of the frequency pattern, further highlighting the convective activity in a shear-organized Stationary Band Complex (Corbosiero & Molinari, 2002; Willoughby et al., 1982).

In addition to shear, another large-scale influence on rainband azimuthal organization is storm motion, which causes preferential frictional convergence and updraft initiation in the right-of-track quadrants (Corbosiero & Molinari, 2003; S. S. Chen et al., 2006). Corbosiero and Molinari (2003) found that track-relative organization

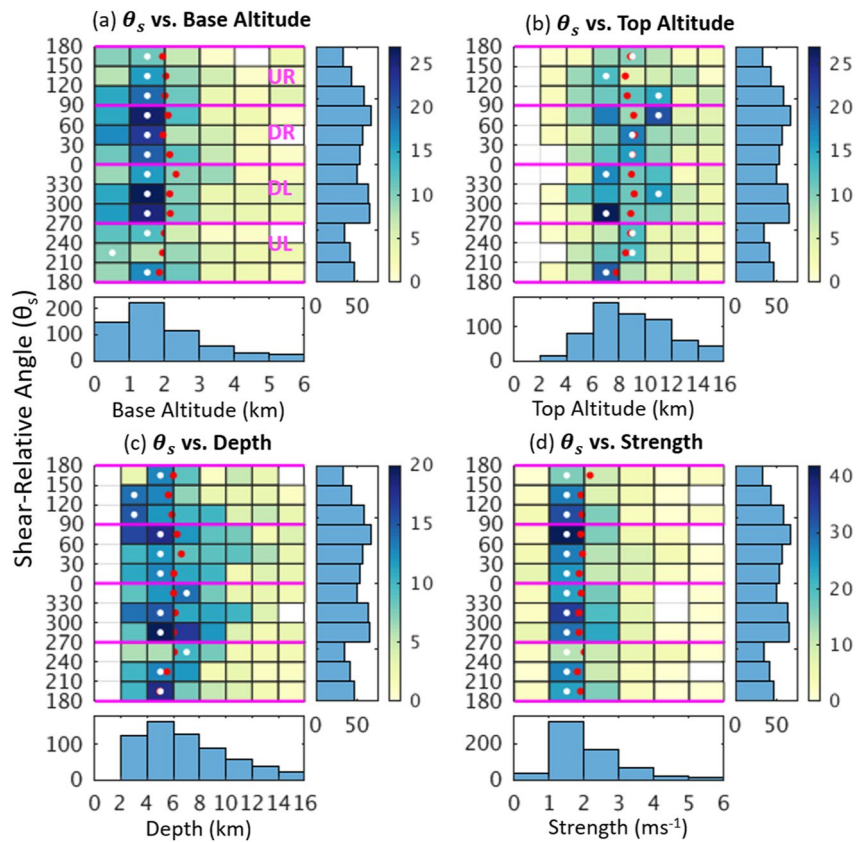


Figure 4. As in Figure 2, but for updraft shear-relative angle ($^{\circ}$) versus (a) updraft base altitude, (b) updraft top altitude, (c) updraft depth, and (d) updraft strength. White and red dots indicate the mode and mean, respectively, of the distribution within each ordinate bin.

only occurs when the storm motion is sufficiently fast ($>3 \text{ ms}^{-1}$) and the shear magnitude is sufficiently weak ($<5 \text{ ms}^{-1}$). To assess this potential impact, Figure 3c plots the track-relative angle versus normalized radius for observation periods with a shear magnitude $<4 \text{ ms}^{-1}$, and Figure 3d further restricts this subset to only include track magnitudes $>3 \text{ ms}^{-1}$. Along with the single-dimension track-relative histogram, a peak in updrafts occurs in the left-of-track half of the storm. But these updrafts, along with those in the right-of-track quadrants, have varying radii and much less organization when compared to the shear-relative plots. The lack of organization in weak shear cases indicates that the track is not playing a significant role in aligning the rainband convective updrafts in our dataset; albeit, low data counts for weak shear cases may partially explain the weak signal. Given the importance of shear based on these findings and previous studies, we focus for the rest of this study only on convective updrafts in moderate-to-strong shear ($>4 \text{ ms}^{-1}$) cases to highlight shear-relative patterns in updraft characteristics.

Azimuthal variations in updraft size and strength are also present in the dataset. Figure 4 shows these variations with shear-relative azimuth, along with the modes and averages of the distributions at each azimuthal bin. As opposed to previous figures, this figure includes the averages because they have more apparent variations in azimuth than in radius across the storm. Figure 4a shows that the modal base altitude is less than 2 km and the average is $\sim 2 \text{ km}$ at all azimuths. This average base reaches its highest value (2.3 km) immediately downshear ($330\text{--}0^{\circ}$), which will be a pertinent finding for later discussions. Meanwhile, the updraft top altitudes (Figure 4b) show scattered modal values at all azimuths. The mean updraft top remains close to 9 km throughout the downshear quadrants ($270\text{--}0^{\circ}$, $0\text{--}90^{\circ}$), while upshear, the mean updraft has lower tops, with a minimum occurring at $180\text{--}210^{\circ}$ of $\sim 7.8 \text{ km}$. A two-sample Kolmogorov–Smirnov (KS) test (Simard & L'ecuyer, 2011) is used to evaluate the statistical significance of different distributions as they occur around the storm. All distribution differences discussed are statistically significant at the $\alpha = 0.95$ level. The distribution of updraft depths (Figure 4c) is wider in the downshear-right (DR) and DL quadrants compared to those distributions upshear. While the modes

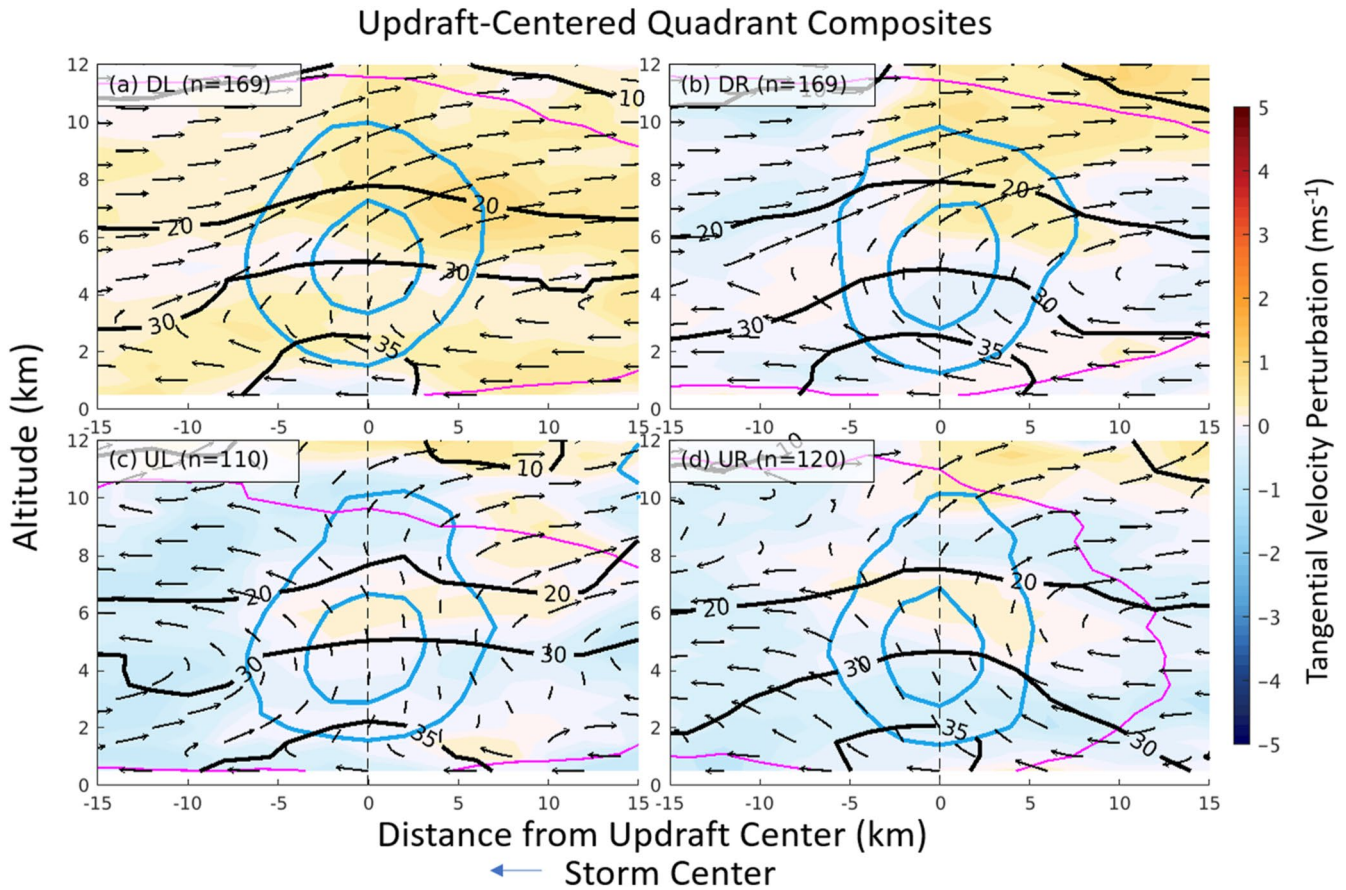


Figure 5. Composite radial cross sections of updrafts in each shear-relative quadrant: (a) downshear-left (DL), (b) downshear-right (DR), (c) upshear-left (UL), and (d) upshear-right (UR). Composites are radially centered on the updraft centroid. Normalized vertical velocity contours are drawn in blue at intervals of 0.5 and 1, where the updraft threshold for each mission normalizes velocities. The flow along the radial and vertical directions is shown as streamline vectors. Tangential velocity perturbations are shaded. Reflectivity contours are drawn in black at 10, 20, 30, and 35 dBZ. The magenta contour outlines locations with <50% of data missing from the cross sections included in the composite. The number of cross sections, n , in each composite is shown.

do not change greatly from upshear to downshear, slightly deeper averages do occur downshear. In Figure 4d, the modal strength remains steady at $1\text{--}2\text{ ms}^{-1}$. All quadrants demonstrate a similarly shaped distribution, with perhaps the exception of a wider distribution in the DL quadrant. Directly upshear ($150^{\circ}\text{--}210^{\circ}$), the average strength appears greatest, but this increase may be the result of a smaller sample size. On the whole, convective updrafts more frequently occur in the downshear storm half, and these updrafts have greater depths and higher tops than those upshear.

5. Total Kinematics of Updraft Elements

5.1. Quadrant-Averaged Composites

The previous statistics show the variety of different rainband updraft characteristics across several storms. To better understand the processes associated with these updrafts, we need to examine their full kinematic structures. We now analyze these kinematics in cross sections centered around the updraft elements and composited for each shear-relative quadrant. The updraft-centered composites are formed by using the vertical-velocity-weighted centroid of each updraft as an anchor to cut a radial cross section. Tangential wind perturbations are calculated by subtracting from each point a moving, azimuthal average that spans $\pm 45^{\circ}$ from the azimuthal coordinate. In this manner, the wavenumber-1 and -2 asymmetries in the tangential velocity are removed. Figure 5 shows updraft-centered composites of the radial and vertical velocities, tangential velocity perturbation, and reflectivity for each shear-relative quadrant.

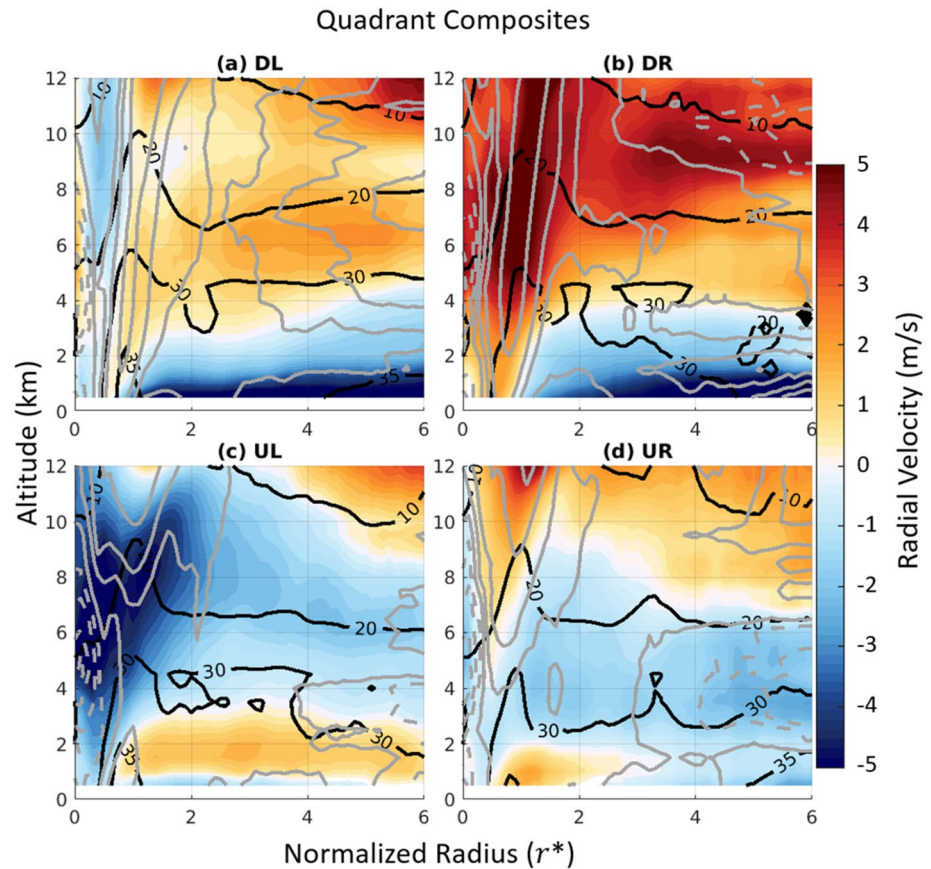


Figure 6. Total quadrant composite cross sections in each shear-relative quadrant: (a) downshear-left (DL), (b) downshear-right (DR), (c) upshear-left (UL), and (d) upshear-right (UR). The radial dimension is put into the normalized radius coordinate r^* . The radial motion is shaded with negative velocities traveling toward the storm center. Positive (negative) vertical velocities are drawn in solid (dashed) gray contours at intervals of 0.25 ms^{-1} . Reflectivity is shown in black contours at 10, 20, 30, and 35 dBZ.

Each updraft-centered quadrant composite shows a unique radial and vertical circulation pattern. First, an in-up-out signature is present in the downshear quadrants (Figures 5a and 5b). The UL quadrant has a mixed out-up-in and out-up-out circulation (Figure 5c). A weaker in-up-out signal also exists on the radial outward portion of the updraft average composites in the UL. The UR has a mixed in-up-in and in-up-out circulation (Figure 5d). In addition, each shear-relative composite has a positive tangential wind perturbation that overlaps the turn from upward flow to upper-level outflow. The perturbations in the UR and DR quadrants are possibly the midlevel tangential jet observed in convective rainbands from previous studies (e.g., Barnes et al., 1983; Didlake & Houze, 2013a; Hence & Houze, 2008). The DL has a widespread area of positive tangential wind perturbation, possibly tied to horizontally broad mesoscale inflow and uplift often seen in the stratiform region of a shear-aligned rainband complex (Didlake & Houze, 2013b; Didlake et al., 2018). These tangential wind perturbations are presented to provide the full kinematic fields of the selected updrafts. They have a complex configuration that will be further examined in a future study.

The updraft-centered radial/vertical circulation patterns can best be understood in the context of the background vortex flow. To obtain this context, total quadrant averages are calculated from all data in each mission, irrespective of updraft frequency and location. These data are then normalized using the defined r^* radial coordinate for each mission. The quadrant composites for reflectivity, radial velocity, and vertical velocity are shown in Figure 6.

The total quadrant composites show clear differences between the downshear (Figures 6a and 6b) and upshear (Figures 6c and 6d) quadrants. The downshear quadrants have strong ($< -5 \text{ ms}^{-1}$), substantial low-level inflow layers outside of the eyewall at $1r^*$, which is marked by clear maxima in upward velocity and reflectivity. The

inflow layer depth (i.e., the altitude at which radial velocity reaches $u = 0$) is about 4 km throughout the DR quadrant, but this layer depth decreases to ~ 3 km in the DL quadrant, particularly between 2 and $4r^*$ where updrafts are most frequent (cf. Figure 2). Above the inflow layer, radial outflow is prominent in both quadrants. Unlike the downshear quadrants, the UL quadrant has low-level outflow between 1 and 3 km altitude, with a shallow inflow layer beneath. Above the outflow layer is a midlevel inflow layer that extends to ~ 12 km altitude. Lastly, the UR displays a low-level outflow layer similar to the UL at smaller radii ($1-2r^*$), but weak inflow occupies the lower levels at larger radii.

The total quadrant composites overall display a radial velocity wavenumber-1 asymmetry expected for TCs experiencing moderate-to-strong environmental wind shear (e.g., Bender, 1997; Frank & Ritchie, 1999, 2001; Jones, 1995; Reasor et al., 2013; Rogers et al., 2013; Zhang et al., 2013). A sheared vortex tends to develop a vertical tilt that is pointed in the downshear-to-downshear-left direction. As a result, the vortex generates a balanced secondary circulation response of enhancements of low-level radial inflow downshear, low-level outflow upshear, midlevel inflow upshear, and midlevel outflow downshear, extending from the eyewall to the rainband regions of the storm.

The radial velocities in the updraft-centered composites largely match those in the total quadrant composites. The in-up-out circulation seen in the downshear updrafts aligns with the radial flow profile of the total quadrant composites. In particular, the inflow layer feeding into the updrafts decreases in depth going from DR to DL (Figures 5a and 5b), just as in the quadrant composites (Figures 6a and 6b) and in previous observational studies (Reasor et al., 2013; Rogers et al., 2013; Zhang et al., 2013). The out-up-in circulation seen in the UL updrafts (Figure 5c) aligns in altitude with the low-level outflow and midlevel inflow of the corresponding total quadrant composite (Figure 6c). Given this coordination, we hypothesize that the radial flow patterns of the average updraft circulations are generally guided by the shear-induced asymmetry of the vortex-scale radial flow.

The mixed in-up-in/in-up-out circulation of the UR quadrant (Figure 5d) aligns somewhat with the total quadrant composite (Figure 6d). The quadrant composite exhibits a deep inflow layer underneath broad outflow radially outside of $r^* = 3$, which matches the in-up-out updraft circulation. However, the shift to upper-level outflow at these radii in the quadrant composite occurs nearly 2 km higher than that of the updraft circulation. Overall, there is more variability in the radial flow profile throughout this quadrant composite, as exemplified by the 1 km radial flow shifting from outward to inward around $r^* = 3$. Rogers et al. (2013) and Reasor et al. (2013) describe the UR quadrant as having the most variable kinematic structures. In prior studies of the UR quadrant, anomalous sinking motion due to shear-vortex interactions was found to suppress convective elements from above, while enhanced low-level moisture enhances convective instability and encourages new convection (Reasor et al., 2013; Rogers et al., 2003). Also, the UR is the most difficult quadrant for obtaining radar echos. The inconsistent structures in our findings may be a result of these two factors.

5.2. Classification of Updraft Circulation Patterns

The quadrant composites provided a first look at the dominant convective-scale circulation patterns throughout a TC, but circulation variations within each quadrant may be obscured by the composite averaging. To better capture the varying characteristics of the radial/vertical velocity circulations, we derive an objective classification scheme that delineates common circulation patterns associated with rainband convective updrafts. Four idealized circulations are identified and illustrated in Figures 7a–7d. The four circulation types are defined as (1) in-up-in, (2) out-up-out, (3) in-up-out, and (4) out-up-in.

To quantitatively define each circulation, four measurements are taken of the kinematics at and around the updraft. First, a radial cross section is taken through the updraft centroid. In this cross section, two boxes are drawn that split the updraft along its centroid altitude, with the top box reaching the updraft top altitude and the bottom box reaching the updraft bottom altitude (Figures 7e–7h). The radial bounds of the boxes extend out to ± 10 km from the centroid in the radial direction. Radial velocity and azimuthal vorticity are then obtained or calculated for each point and averaged over the domain of each box, resulting in four deterministic measurements: top velocity, top vorticity, bottom velocity, and bottom vorticity. Different combinations of each measurement across the two boxes ideally describe the four circulation types (as shown in Figures 7a–7d). However, rather than using strict Boolean expectation ranges for each classification, we use a probabilistic method to allow a small amount of flexibility within each expected measurement range, which leads to a better overall scheme.

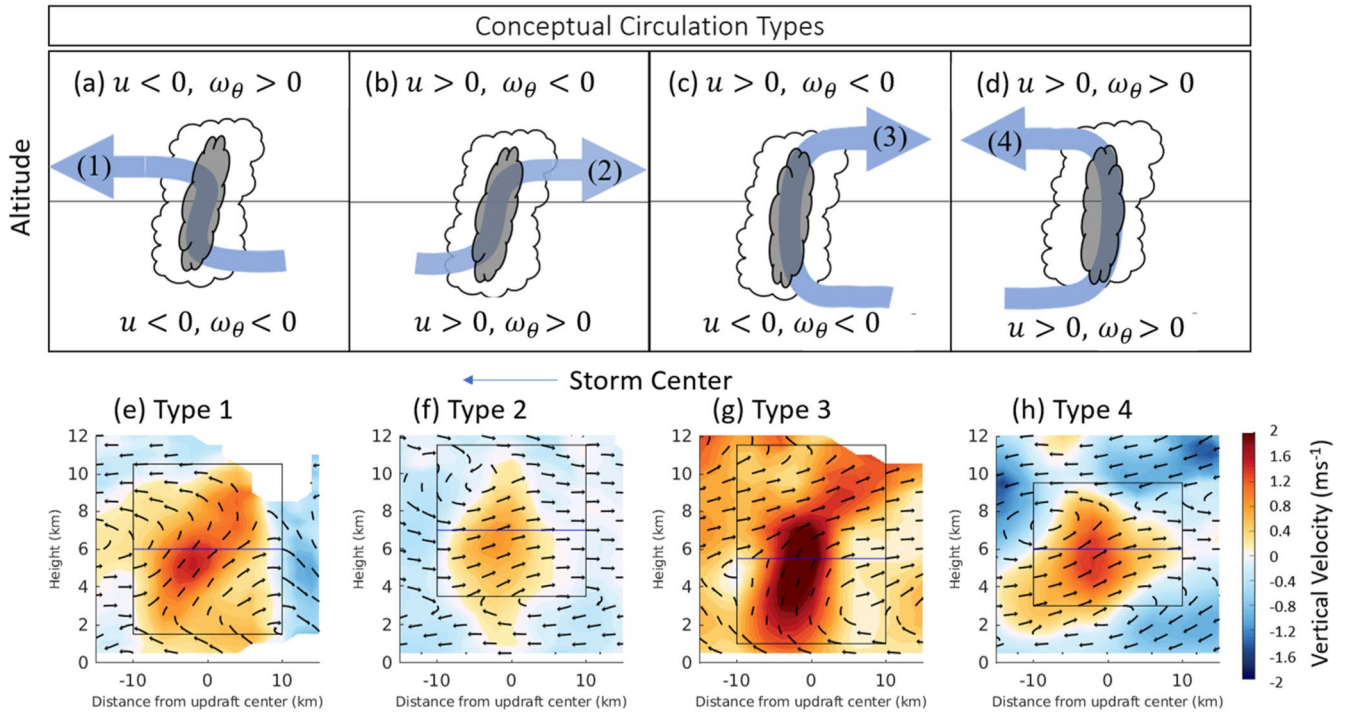


Figure 7. (a–d) Schematic of the four circulation types as defined by the circulation classification algorithm for rainband convective updrafts. Updrafts are sketched in gray and embedded in an outlined cloud. Idealized streamlines for each circulation type are shown in light blue. The expected signs for the azimuthal vorticity (ω_θ) and radial velocity (u) are indicated in the upper and lower boxes. (e–h) Example convective updraft cross sections for each classification type. Streamline vectors depict the radial and vertical flow. Shading shows the vertical velocity. Upper and lower boxes are divided at the updraft centroid and bounded by top and base altitudes and ± 10 km from the updraft center.

We define an arbitrary probability density kernel (PDK) for each expectation value, Y_{ji} (shown in Table 2), where j and i are the circulation type and measurement indices, respectively. The measured value (X_i), either velocity or vorticity, is then used to assign a sub-probability p_{ji} , calculated from the PDK function of a Gaussian distribution, given by

$$p_{ji} = \begin{cases} \frac{1}{b\sqrt{2\pi}} \int_{-\infty}^{X_i} e^{-\left(\frac{x-a}{4b}\right)^2} dx & \text{for } Y_{ji} < 0 \\ \frac{1}{b\sqrt{2\pi}} \int_{X_i}^{\infty} e^{-\left(\frac{x+a}{4b}\right)^2} dx & \text{for } Y_{ji} > 0 \end{cases}, \quad (1)$$

where a and b are Gaussian distribution parameters (the mean and standard deviation, respectively). The values of a and b are chosen to be equal to one; this choice ensures that the calculations do not produce rounding errors in the following procedure.

Table 2

Table of the Expectation Value (Y_{ji}) for Each of the Four Measured Quantities (X_i) and Classification Types Used for the Circulation Type Algorithm

Measurement	Expectation (Y_{1i})	Expectation (Y_{2i})	Expectation (Y_{3i})	Expectation (Y_{4i})
Top radial velocity (X_1)	$Y_{11} < 0$	$Y_{21} > 0$	$Y_{31} > 0$	$Y_{41} < 0$
Top azimuthal vorticity (X_2)	$Y_{12} > 0$	$Y_{22} < 0$	$Y_{32} < 0$	$Y_{42} > 0$
Bottom radial velocity (X_3)	$Y_{13} < 0$	$Y_{23} > 0$	$Y_{33} < 0$	$Y_{43} > 0$
Bottom azimuthal vorticity (X_4)	$Y_{14} < 0$	$Y_{24} > 0$	$Y_{34} < 0$	$Y_{44} > 0$

Note. The indices j and i represent the circulation type and measurement indices, respectively.

The sub-probability acts as a weight, ranging between 0 and 1. For a given cross section, p_{ji} is calculated for each combination of the four measurements and classifications. The products of the sub-probabilities for each measurement expectation are calculated for each potential type, given by

$$P_j = p_{j1} \times p_{j2} \times p_{j3} \times p_{j4}. \quad (2)$$

Of the four values of P_j , the greatest value, $P_{j_{\max}}$, determines the circulation type, assigned as j_{\max} for a given cross section. Using this method, the classification scheme can forgive a single measurement for a classification type that does not match the sign of the expectation value and still punish the classification types that are not appropriate for that updraft cross section. This methodology was tested by analyzing the cross section velocity fields and subjectively assigning a classification type. The qualitative analysis and the quantitative algorithm described above compared closely to each other. Figures 7c–7h show example cross sections for each classification type.

5.3. Updraft Characteristics for Each Circulation Type

Figure 8 shows the joint frequency plots of location, size, and strength versus the circulation type. As seen in the single-dimension type frequency counts, the type 3 (in-up-out) circulation type is by far the most frequent. Type 2 (out-up-out) is the second most frequent and is closely followed by types 1 (in-out-in) and 4 (out-up-in).

Starting at $\theta_s = 120^\circ$ and going downwind in Figure 8a, the type 3 updraft frequency increases sharply and persists until $\theta_s = 270^\circ$ where the frequency notably decreases. Type 3 updrafts do occur in the upshear quadrants, but the majority occurs downshear. Type 2 updrafts have a high frequency in the DL quadrant and a second narrower peak in the DR at 60° – 90° . This second peak stems from isolated occurrences in six flights from Earl and Michael. Type 1 updrafts are found mostly in the upshear quadrants. Lastly, type 4 updrafts have a narrow distribution that peaks in the UL quadrant.

Figure 8b shows the normalized radius versus circulation type. Type 1 circulations have a frequency peak occurring at 2 – $3r^*$ with a distribution tail extending to $6r^*$. Type 2 updrafts also tend to occur at smaller radii with higher frequencies at 2 – $4r^*$. Type 3 has a narrower distribution peaking at 3 – $4r^*$, while type 4 has a wider distribution with a mode at 4 – $5r^*$.

Figures 8c–8f shows the frequencies of updraft base altitude, top altitude, depth, and strength for each circulation type. Most updraft bases are between 1 and 2 km (Figure 8c). Type 3 updrafts have a higher tendency for base altitudes between 0 and 1 km than other types, and type 2 updrafts have a wide distribution that shows an increased number of high-base-altitude updrafts; this type 2 base altitude distribution is statistically significantly different from the other three distributions. Types 1 and 4 have updraft tops most often between 6 and 8 km, while types 2 and 3 often have updraft tops reaching 8–12 km altitude (Figure 8d). The top altitude distributions of types 2 and 3 are statistically significantly different from those of types 1 and 4. Figure 8e shows that types 1, 2, and 4 updrafts are mostly between 2 and 8 km deep, with a frequency peak between 4 and 6 km. Type 3 updrafts are the deepest updrafts, with depths mostly between 2 and 12 km and a frequency peak between 6 and 8 km. This type 3 depth distribution is statistically significantly different from those of the other three types. The updraft strengths (Figure 8f) show slight variation between circulation types but largely remains between 1 and 2 ms^{-1} . Type 3 updrafts are stronger (1 – 4 ms^{-1}) than all other updraft types, a distribution difference that is also statistically significant. In summary, type 3 updrafts have mostly lower base altitudes, mostly higher top altitudes, deeper extents, and stronger magnitudes than the other types.

Our defined circulation types have been identified in many past studies. The deep and frequent type 3 (in-up-out) updraft is the same as that studied in several observational studies (Barnes & Stossmeister, 1986; Barnes et al., 1983; Barnes & Powell, 1995; C. K. Yu et al., 2018; Didlake & Houze, 2009, 2013b; Hence & Houze, 2008; May 1996; Powell, 1990a, 1990b; Samsury & Zipsper, 1995; Tang et al., 2018) and modeling studies (Li & Wang, 2012a; Moon & Nolan, 2015). These prominent features were generally found in the principal rainband of an organized rainband complex and often exhibited deep radial inflow like those currently presented. Type 1 (in-up-in) updrafts tended to be observed in distant outer rainbands that propagated radially outward like squall lines (Barnes et al., 1991; C. K. Yu & Tsai, 2013; C. K. Yu et al., 2018; Moon & Nolan, 2015; Ryan et al., 1992). Their kinematic and thermodynamic structures in these studies indicated that squall line dynamics (e.g., Didlake & Houze, 2013b) governed the rainband evolution. Moon and Nolan (2015) showed that simulated inner rainbands could also exhibit type 1 updrafts (see their Fig. 15), but these updrafts were not tall, reaching only up

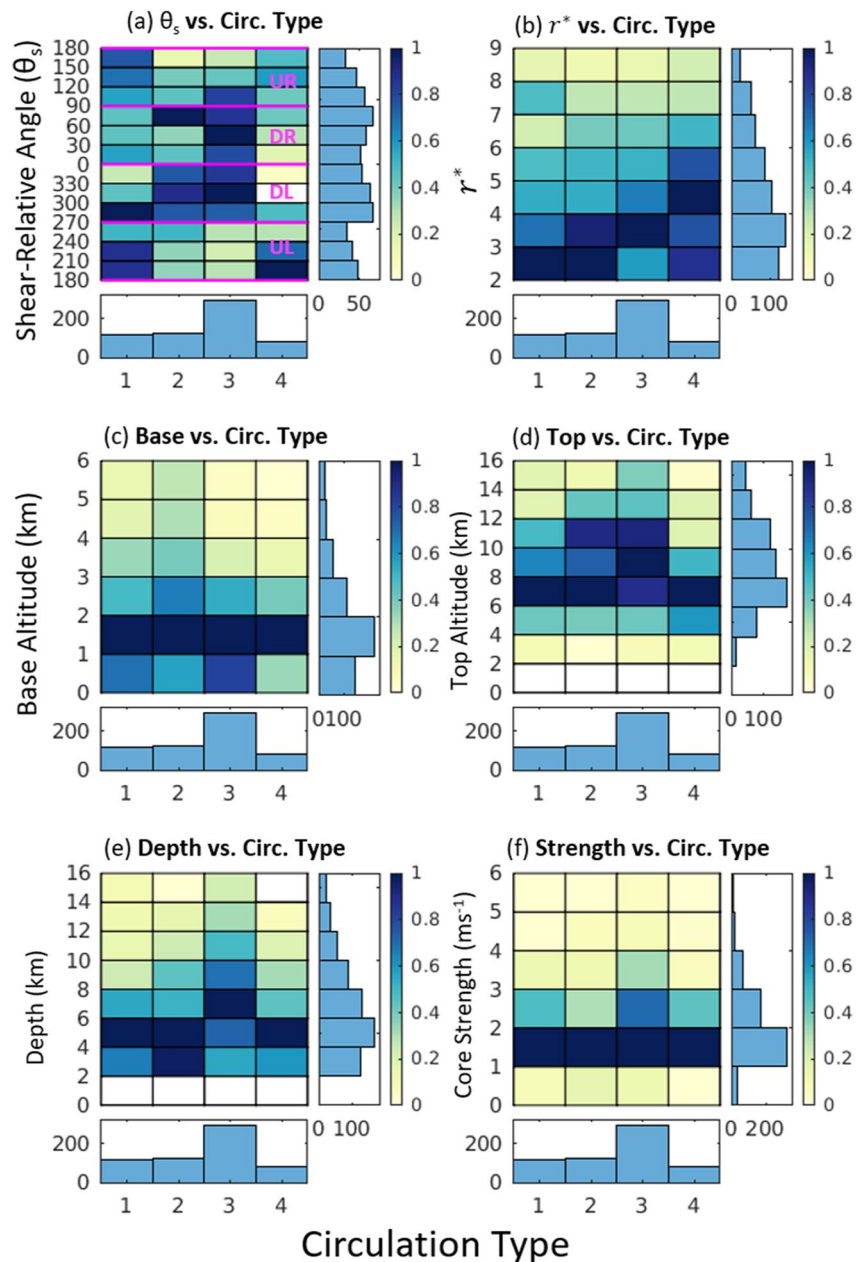


Figure 8. As in Figures 2 and 3 but for circulation classification type versus (a) shear-relative angle ($^{\circ}$), (b) normalized radius (r^*), (c) updraft base, (d) updraft top, (e) updraft depth, and (f) strength. Each column has been normalized so that the deepest color in each column corresponds to the maximum value in that column.

to 4 km altitude. Tang et al. (2014) studied convective cells within the principal rainband (located at intermediate radii) and found similar circulations to types 1 and 3. Type 2 circulations were found in Didlake and Houze (2013b) and Didlake et al. (2018), particularly in rainband regions with prominent surrounding stratiform precipitation. Didlake and Houze (2013b) showed updrafts with elevated bases (~ 3 km) and shallow depths (~ 4 km), while Didlake et al. (2018) showed rainband updrafts with a 0.5 km base and 13 km depth.

5.4. Azimuthal Variations in Updraft Size, Location, and Circulation Type

Azimuthal variations in updraft characteristics were first noted in their frequency distributions and averages (Figure 4) and then further examined when stratifying by circulation type (Figure 8). In a more detailed analysis,

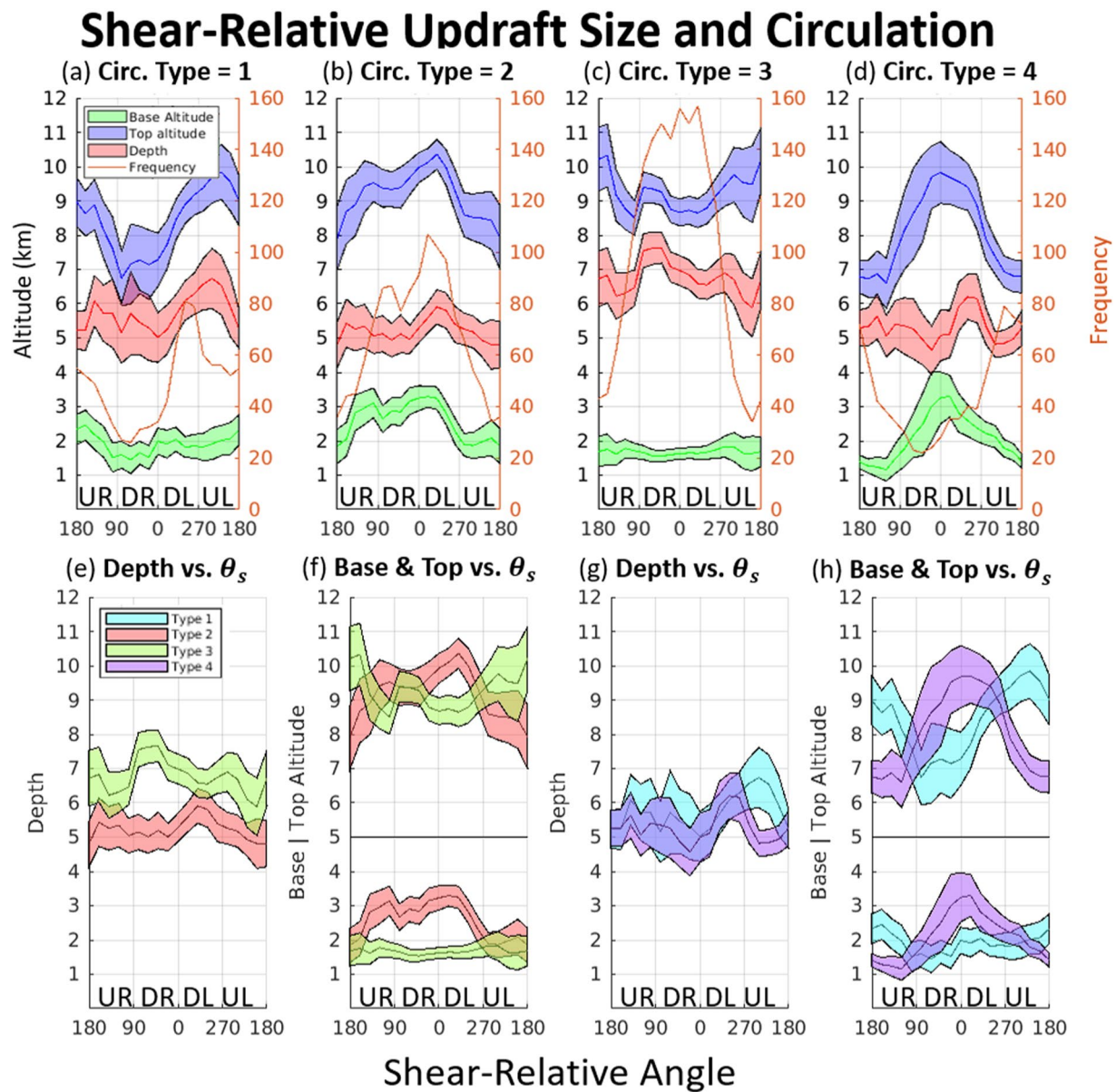


Figure 9. (a–d) Average values of updraft base altitude, depth, and top altitude as a function of shear-relative angle ($^{\circ}$) separated by circulation type. Values are calculated every 20° in a moving azimuthal average over $\pm 30^{\circ}$. Shaded regions represent the statistical significance confidence intervals at the 95% level. The frequency of updrafts is shown in red along the right-hand-side axes. Shear-relative quadrants are labeled at the bottom, moving cyclonically from left to right. (e–f) Same as (a–d) but stratified by updraft depth in (e) and base and top in (f) for types 2 and 3. (g–h) Same as (e–f) but for types 1 and 4.

Figure 9 plots moving averages of the updraft base altitude, top altitude, and depth with the shear-relative angle for each circulation type. These averages provide a snapshot of how the aggregate of updrafts evolves as they propagate around the storm. In addition, confidence intervals at the 95% level (calculated using a two-sided Student's *t*-test) are shown to determine the statistical significance of the differences between each average.

As shown in Figure 8a, types 2 and 3 are most frequent in the downshear quadrants, with notable occurrences of type 3 in the UR quadrant. Type 2 updrafts (Figure 9b) exhibit a minimum base altitude of 2 km in the UL and UR quadrants, and a maximum of ~ 3 km altitude in the DR and DL quadrants. Meanwhile, type 3 updrafts (Figure 9c) exhibit an average base altitude that does not change appreciably across the entire storm. In comparison, type 2 base altitudes (~ 3 km) are statistically significantly higher than those of type 3 (~ 1.5 km) in the downshear quadrants (Figure 9f). Figure 9e is consistent with Figure 8e, showing that type 3 depths (reaching 7.5 km)

are statistically significantly higher than those of type 2 (reaching 6 km), particularly in most of the downshear quadrants. The updraft tops for types 2 and 3 (Figure 9f) reveal a more complex pattern than that suggested by Figure 8d. The top altitudes for types 2 and 3 are coincident in the DR quadrant at 9.5 km, but downwind, the type 2 top increases to become statistically significantly higher in the DL quadrant. In fact, both the depth and top altitude of type 2 increase, while the type 3 depth and top both decrease going from DR to DL, where both types reach their peak frequency. This interesting finding indicates an opposite pattern of evolving type 2 and 3 characteristics.

Types 1 and 4 are most frequent in the upshear quadrants, except for the type 1 spike at 300° – 270° . Type 1 updrafts (Figure 9a) have an average base altitude near 2 km in the upshear quadrants. Going from DR to UL, the average depth grows from 5 to 6.5 km, and the average top grows from 7 to 9.5 km. Figures 9g and 9h shows the comparisons between types 1 and 4. In the upshear quadrants, type 4 updrafts exhibit a lower base altitude (1.5 km), slightly lower depth (~5.5 km), and lower top altitude (7 km) than those of type 1.

A pattern emerges from these analyses that suggest a relationship between the vortex-scale shear-induced asymmetry of the background radial flow and the dominant circulation types and characteristics. For each circulation type, the radial flow direction of the upper branch at the updraft top altitude tends to match the radial flow direction at that altitude in the total quadrant composites (Figure 6). Types 2 and 3, dominant in the downshear quadrants, have radial outflow at their updraft tops between 6 and 12 km altitude, and this matches the 6–12 km radial outflow in the downshear quadrant composites. Types 1 and 4, dominant in the upshear quadrants, have radial inflow at their updraft tops near 6–8 km altitude, and this matches the 6–8 km radial inflow in the upshear quadrant composites.

A similar comparison can be made when examining the altitudes and radial flow of the updraft bases. In the downshear quadrants, type 3 has low-level inflow and lower base heights, matching the low-level inflow layer in the downshear quadrant composites. Type 2 has low-level outflow and higher base altitudes, which more likely corresponds to the elevated outflow layer in the downshear composites. This similarity is most notable for DL updrafts at less than $3r^*$ radius, given that the inflow-to-outflow switch in the quadrant composite is near 3 km altitude, which is the average base height at the type 2 frequency peak. Upshear, type 4 has outflow with lower base heights spanning 1–2.5 km, which roughly aligns with the altitudes of the supergradient outflow layer of the upshear quadrant composites. The slightly higher base altitudes of type 1 updrafts suggest that these updrafts likely occur above the outflow-to-inflow switch between 2 and 3 km altitude in the quadrant composites. The weaker radial velocities in the UR quadrant likely indicate more varying radial flow directions, which is supported by the increased spread in the circulation types occurring here (Figure 8a).

We hypothesize that this overall relationship is a result of the vortex-scale asymmetry controlling the dominant radial flow of the convective-scale updraft circulations. The vertical profile of the vortex radial flow is dynamically shaped by vortex interaction with the environmental wind shear. Given this, the circulation type of an individual updraft would then be determined by its shear-relative location, base altitude, and top altitude.

The updraft characteristics and circulation patterns are also consistent with the convective evolution of updrafts propagating downwind within a shear-organized rainband complex. Rainband convection begins to form in the UR quadrant as denoted by the increase in updraft frequency between 150° and 70° , predominantly type 3. As these updrafts travel downwind, they intensify, as shown by the type 3 depths, and top altitudes are shown to increase from UR to DR. Similar findings are presented by Li and Fang (2019) in their study of convection and buoyancy, with the convection that is directly downshear experiencing more buoyancy. Then, as the convection travels further downwind, the convective cells age and prominent stratiform precipitation begins to form early in the DL quadrant (Didlake & Houze, 2013b; Hence & Houze, 2012a).

An opposite pattern of types 2 and 3 updraft top and depth is observed here. This pattern may be explained by a gradual exchange in the populations of the two updraft types. In particular, a portion of the deeper and taller updraft population transitions from type 3 to type 2. During this transition, some of the in-up-out (type 3) circulations experience reversed radial flow in its lower branch due to a combination of a shrinking low-level inflow layer and increased low-level downdrafts from evaporation within the growing stratiform precipitation. The vortex-scale shear-induced asymmetry in the radial flow causes the low-level inflow layer depth to steadily shrink going from DR to DL. For an updraft population being advected downwind, a shrinking inflow layer would result in increasing type 2 frequencies, given that an unchanging updraft base would gradually be displaced from the

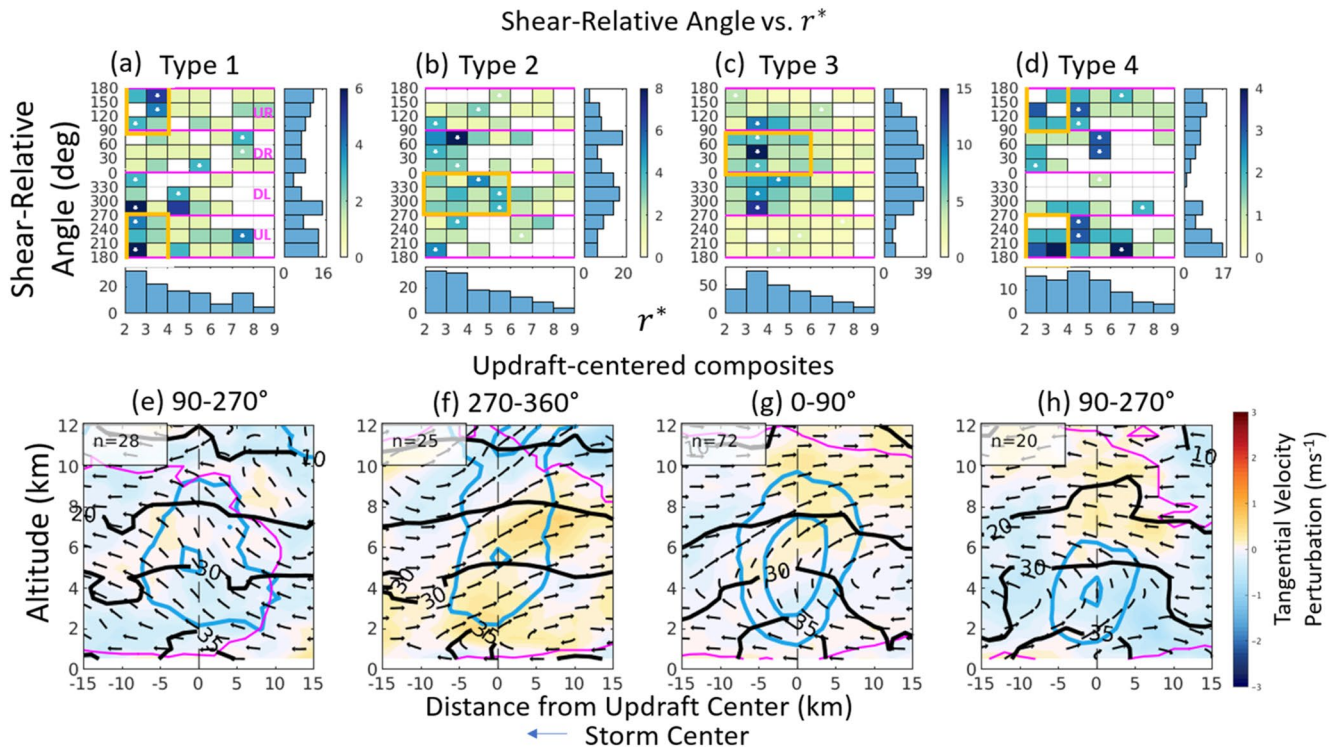


Figure 10. (a–d) As in Figure 3 but stratified by circulation type. (e–f) As in Figure 5 but with cross section composites using only updrafts within the radial and azimuthal ranges denoted by the colored boxes in the first row and corresponding to the circulation type directly above.

low-level inflow layer. At the same time, the DL quadrant generally is where many aging convective cells begin to collapse and low-level downdrafts from evaporation become more prevalent. These downdrafts would then erode the updraft bases of some type 3 updrafts, elevate the cloud base above the inflow layer, and turn them into type 2 updrafts. Both of these scenarios are consistent with the type 2 base altitudes remaining higher than those of type 3 throughout the DR and DL quadrants (Figure 9d).

We now further examine frequency distributions and cross sections of the updraft types presented previously. Figures 10a–10d is similar to Figure 3, showing the updraft frequencies by shear-relative azimuth versus normalized radius for a given circulation type, and now with regions highlighted by boxes. Figures 10e–10h presents the cross section composites from updrafts identified by the boxes for each circulation type. These box regions were specifically selected to further illustrate details of the updraft characteristics.

Type 3 updrafts are found primarily in a downshear band located between 3 and 4 r^* (Figure 10c). Consistent with previous analyses in Figure 8, these updrafts are the strongest updrafts of the four circulation types, as demonstrated by the intense and large vertical velocity structure in Figure 10g. The reflectivity structure is marked by bell-shaped 30 and 35 dBZ contours, which suggest discrete, strong convective cells.

Among all quadrants, type 2 updrafts occur most frequently in the DL quadrant (Figure 10b). Their composite cross section (Figure 10f) displays an elevated base altitude, large vertical depth, and high top altitude, similar to what was shown statistically in Figure 8. The 30 dBZ reflectivity contour is more horizontal than that seen in the type 3 cross section, which suggests more surrounding stratiform precipitation. Radial velocities show a shallow inflow layer below 2 km that shifts to outflow above this altitude, which is the low-level outflow that is part of the type 2 circulation.

As described earlier, a type-3-to-type-2 transition in the updraft population likely occurs in the downshear quadrants as a result of the inflow layer decreasing below the updraft base and/or low-level downdrafts elevating the updraft base above the background inflow layer. This behavior is consistent with the cross sections in Figures 10f and 10g where type 3 updrafts in the DR quadrant have an updraft base within the moderately deep inflow layer, while type 2 updrafts have a base altitude that is above a shallow inflow layer.

Figure 10a shows that type 1 updrafts in the upshear quadrants are mostly occurring between 2 and $4r^*$. An examination of individual cases (not shown) showed that these upshear type 1 updrafts were often found to be embedded in a larger rainband complex. Figure 10d shows type 4 updrafts in the upshear quadrants occur with near-constant frequencies at all radii less than $6r^*$. Comparing to the composite cross section of type 1, type 4 has a lower updraft top, consistent with Figure 8d. The reflectivity structure is comprised of bell-shaped contours, more so than for type 3, possibly indicating that type 4 circulations are associated with more isolated convective cells that grow and dissipate in the upshear quadrants. Based on this analysis, type 4 updrafts may represent shallow, isolated convective cells frequently observed in the upshear, upwind beginning of a shear-organized rainband complex. The composite cross sections reinforce the findings in the previous figures. Wherever each updraft circulation type is most frequent, its radial flow is generally aligned with the vortex-scale shear-induced radial flow pattern at the updraft base and top altitudes.

6. Conclusions

This study examines rainband convective updrafts' kinematic and reflectivity characteristics observed by airborne Doppler radar across 10 years of Atlantic and central Pacific basin hurricanes. Using an objective updraft clustering algorithm, statistics were recorded from each updraft, including measurements of the updraft size, strength, convective-scale secondary circulation, radial location, and azimuthal location relative to the 200–850 hPa environmental wind shear vector. These statistics were analyzed to determine the variety of convective updrafts present in a variety of hurricane-strength TCs.

On average, convective rainband updrafts become deeper and stronger with increasing radius, likely due to increasing CAPE with radius (Bogner et al., 2000). When analyzed with respect to the environmental wind shear vector, a wavenumber-1 asymmetry in updraft frequency appears, with updrafts being more frequent and deeper in the downshear quadrants of the storm and less frequent and shallower in the upshear quadrants. This asymmetry aligns closely in structure and orientation with a typical shear-organized rainband complex (Hence & Houze, 2012a; Riemer, 2016). The radial flow direction near the updraft base and top tend to follow the background vortex-scale radial flow profile, which has a shear-induced wavenumber-1 asymmetry of increased low-level inflow (outflow) and midlevel outflow (inflow) in the downshear (upshear) quadrants of the storm. This asymmetry further appears as a low-level inflow layer of varying depths; in particular, the downshear inflow layer decreases in depth traveling from the downshear-right to downshear-left quadrants, consistent with previous studies (Bender, 1997; Jones, 1995; Reasor et al., 2013; Zhang et al., 2013).

We further analyzed the observed secondary circulations (radial and vertical velocity) associated with the convective updrafts by implementing a kinematic classification system that sorts the flow patterns around each updraft into four types: (1) in-up-in, (2) out-up-out, (3) in-up-out, (4) out-up-in. The frequencies, distributions, and structures of these circulation types revealed additional context of the typical rainband convective updrafts.

Figure 11 summarizes the findings in a conceptual model. The plan view reflectivity outlines a shear-organized rainband complex that exhibits growing and mature convective cells in the right-of-shear half, which then travel downwind into the left-of-shear half to eventually collapse and transition to stratiform precipitation. Cross sections in different quadrants illustrate the most prominent secondary circulation patterns and reflectivity structures associated with the convective rainband updrafts there. Their characteristics are described as follows:

1. DR (Panel I): Type 3 updrafts are the deepest, strongest, and most frequent updraft circulation here in the DR quadrant and the overall storm. These updrafts form from a deep layer (4 km) of low-level inflow in the background vortex. Tall, clear reflectively towers accompany the convective updrafts
2. DL (Panel II): Both types 2 and 3 are prominent. Type 3 updrafts have a lower base altitude within the 3-km-deep low-level background inflow layer. In comparison, type 2 updrafts have a higher base altitude above the inflow-to-outflow transition of the background profile. Reflectivity towers are embedded in heavier surrounding precipitation, consistent with the increasing stratiform nature of the larger rainband complex
3. UL (Panel III): Types 1 and 4 are the most frequent circulations, as these types have radial inflow at their top altitudes which matches the background radial inflow. Type 1 tops are notably higher than those of type 4. Updrafts occurring here have a circulation type that depends largely on their base height. Lower base heights tend to be embedded in a low-level background radial outflow layer, while higher base heights tend to occur in background radial inflow

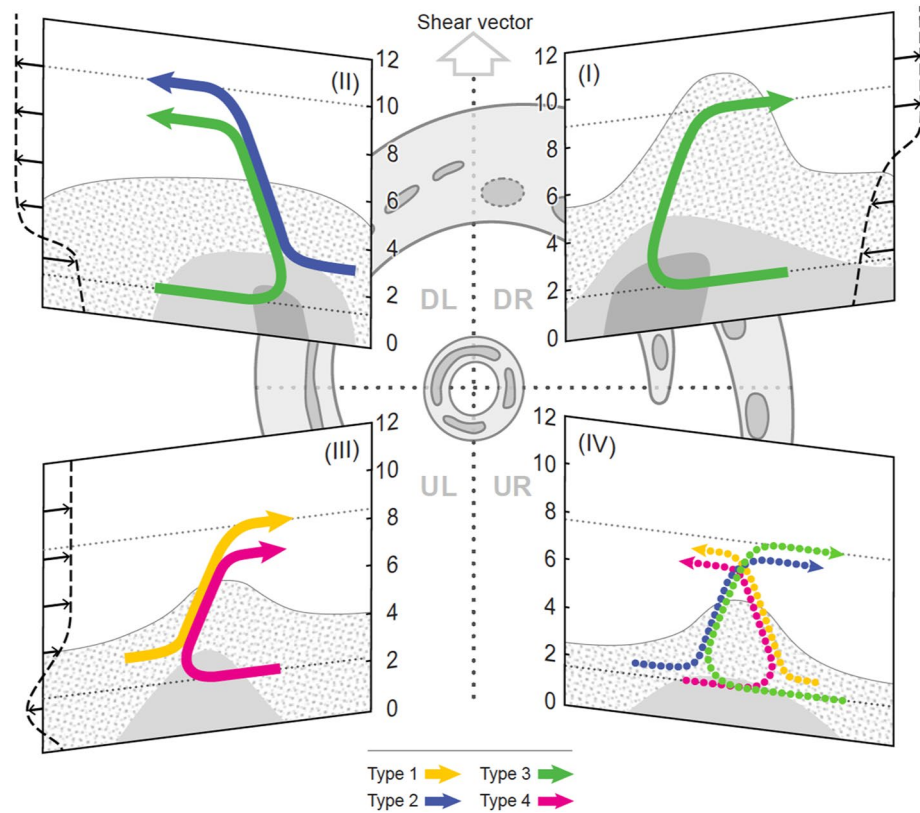


Figure 11. Conceptual model of convective updraft characteristics in an organized rainband complex. The plan view of the rainband complex is shown by reflectivity contours of 20 and 35 dBZ. The environmental wind shear vector points upward (gray arrow) and defines the shear-relative storm quadrants. Panels I–IV show radial cross sections (altitude in km) in each of the shear-relative quadrants. The colored streamlines represent the prominent updraft circulations (each color corresponding to one of the circulation types) present in each quadrant of the storm. Arrows at the panel edge show the vortex-scale inflow and outflow. The dotted streamlines and lack of radial flow arrows in panel IV indicate weaker signals of each circulation type. Reflectivity contours in the cross sections are drawn at 20, 30, and 35 dBZ. Adapted from Didlake and Houze (2013b).

4. UR (Panel IV): The UR is the most variable quadrant, with all circulation types occurring at similar frequencies. Traveling downwind, types 1 and 4 have decreasing frequencies and types 2 and 3 have increasing frequencies, with type 3 being the most frequent overall. The background radial flow profile is the most variable in this quadrant. The updrafts form isolated reflectivity towers, consistent with the convective cell initiation in the upwind portion of the larger rainband complex

The alignment of updraft circulation types and the expected vortex-scale radial flow asymmetry in sheared storms leads us to hypothesize that the environmental wind shear is directly influencing the radial flow of the convective-scale rainband updraft circulations. A secondary influence would be the local buoyancy and other convective evolution details (e.g., initiation mechanism, entrainment/detrainment rates) that would determine the top and bottom altitudes of the updraft. Deep, prevalent updrafts in the downshear quadrants most likely have type 3 circulations, like those examined in the principal rainbands of past studies (Barnes et al., 1983; Barnes & Stossmeister, 1986; Barnes & Powell, 1995; C. K. Yu et al., 2018; Didlake & Houze, 2009, 2013b; Hencé & Houze, 2008; May 1996; Powell, 1990a, 1990b; Samsury & Zipser, 1995; Tang et al., 2018).

Interestingly, the depth and top of type 3 updrafts decrease going from the DR to DL quadrants, while simultaneously, the depth and top of type 2 updrafts increase. A possible explanation is that a portion of the deeper and taller updraft population transitions from type 3 (having lower base altitudes) to type 2 (having higher base altitudes). During this transition, downshear updrafts experience a shrinking of the background low-level inflow layer going from DR to DL, and the aging convective updrafts typical of this region experience bottom-up decay

from increased low-level, evaporation-driven downdrafts. Both effects would shift the radial flow at the updraft base from inflow to outflow, consistent with transitioning from type 3 to type 2.

This study ties together the many different characteristics of convective rainband updrafts that have been documented in the literature, both in observational and modeling studies. The results help shed light on how these updraft circulations are organized and what underlying dynamics might contribute to the observed organization. Additional observations with increased spatial and temporal resolution would help to assess the ubiquity of the convective updraft patterns and behaviors seen in this study. Future studies may also include analyzing these updraft patterns in high-resolution numerical models.

Data Availability Statement

The TDR dataset is available from HRD at <https://www.aoml.noaa.gov/ftp/pub/hrd/data/radar/level3/>.

Acknowledgments

We would like to thank George Young, Kelly Lombardo, James Ruppert, Frank Marks, and three anonymous reviewers for their comments and suggestions on this work. We are grateful for Beth Tully and her work on the conceptual model, the last of her excellent contributions to scientific literature in the past 18 years. We would also like to thank John Gamache and Michael Fischer for developing and maintaining the TDR analysis dataset at HRD. We also thank NOAA's Aircraft Operations Center staff, who have collected the TDR data over many years and made such multi-case studies possible. This material is based upon work supported by the National Science Foundation under Award No. AGS-1810869. Any opinions, findings, and conclusions or recommendations expressed in this publication are those of the author(s) and do not necessarily reflect the views of the National Science Foundation.

References

- Alland, J. J., Tang, B. H., Corbosiero, K. L., & Bryan, G. H. (2021a). Combined effects of midlevel dry air and vertical wind shear on tropical cyclone development. Part I: Downdraft ventilation. *Journal of the Atmospheric Sciences*, 78, 763–782. <https://doi.org/10.1175/JAS-D-20-0054.1>
- Alland, J. J., Tang, B. H., Corbosiero, K. L., & Bryan, G. H. (2021b). Combined effects of midlevel dry air and vertical wind shear on tropical cyclone development. Part II: Radial ventilation. *Journal of the Atmospheric Sciences*, 78, 783–796. <https://doi.org/10.1175/JAS-D-20-0055.1>
- Barnes, G. M., Gamache, J. F., Lemone, M. A., & Stossmeister, G. J. (1991). A convective cell in a hurricane rainband. *Monthly Weather Review*, 119, 776–794. [https://doi.org/10.1175/1520-0493\(1991\)119<0776:acciah>2.0.co;2](https://doi.org/10.1175/1520-0493(1991)119<0776:acciah>2.0.co;2)
- Barnes, G. M., & Powell, M. D. (1995). Evolution of the inflow boundary layer of Hurricane Gilbert (1988). *Monthly Weather Review*, 123, 2348–2368. [https://doi.org/10.1175/1520-0493\(1995\)123<2348:eotib>2.0.co;2](https://doi.org/10.1175/1520-0493(1995)123<2348:eotib>2.0.co;2)
- Barnes, G. M., & Stossmeister, G. J. (1986). The structure and decay of a rainband in Hurricane Irene (1981). *Monthly Weather Review*, 114, 2590–2601. [https://doi.org/10.1175/1520-0493\(1986\)114<2590:tsadoa>2.0.co;2](https://doi.org/10.1175/1520-0493(1986)114<2590:tsadoa>2.0.co;2)
- Barnes, G. M., Zipser, E. J., Jorgensen, D., & Marks, F. (1983). Mesoscale and convective structure of a hurricane rainband. *Journal of the Atmospheric Sciences*, 40, 2125–2137. [https://doi.org/10.1175/1520-0469\(1983\)040<2125:macsoa>2.0.co;2](https://doi.org/10.1175/1520-0469(1983)040<2125:macsoa>2.0.co;2)
- Bell, M. M., Montgomery, M. T., & Lee, W.-C. (2012). An axisymmetric view of concentric eyewall evolution in Hurricane Rita (2005). *Journal of the Atmospheric Sciences*, 69, 2414–2432. <https://doi.org/10.1175/JAS-D-11-0167.1>
- Bender, M. A. (1997). The effect of relative flow on the asymmetric structure in the interior of hurricanes. *Journal of the Atmospheric Sciences*, 54, 703–724. [https://doi.org/10.1175/1520-0469\(1997\)054<0703:teorfo>2.0.co;2](https://doi.org/10.1175/1520-0469(1997)054<0703:teorfo>2.0.co;2)
- Black, M. L., Burpee, R. W., & Marks, F. D. (1996). Vertical motion characteristics of tropical cyclones determined with airborne Doppler radial velocities. *Journal of the Atmospheric Sciences*, 53(13), 1887–1909. [https://doi.org/10.1175/1520-0469\(1996\)053<1887:vmcotc>2.0.co;2](https://doi.org/10.1175/1520-0469(1996)053<1887:vmcotc>2.0.co;2)
- Bogner, P. B., Barnes, G. M., & Franklin, J. L. (2000). Conditional instability and shear for six hurricanes over the Atlantic Ocean. *Weather and Forecasting*, 15, 192–207. [https://doi.org/10.1175/1520-0434\(2000\)015<0192:ciasfs>2.0.co;2](https://doi.org/10.1175/1520-0434(2000)015<0192:ciasfs>2.0.co;2)
- Bu, Y. P., Fovell, R. G., & Corbosiero, K. L. (2017). The influences of boundary layer mixing and cloud-radiative forcing on tropical cyclone size. *Journal of the Atmospheric Sciences*, 74, 1273–1292. <https://doi.org/10.1175/JAS-D-16-0231.1>
- Chen, S. S., Knaff, J. A., & Marks, F. D., Jr. (2006). Effects of vertical wind shear and storm motion on tropical cyclone rainfall asymmetries deduced from TRMM. *Monthly Weather Review*, 134(11), 3190–3208. <https://doi.org/10.1175/MWR3245.1>
- Chen, Y., & Yau, M. K. (2001). Spiral bands in a simulated hurricane. Part I: Vortex Rossby wave verification. *Journal of the Atmospheric Sciences*, 58, 2128–2145. [https://doi.org/10.1175/1520-0469\(2001\)058<2128:sbiash>2.0.co;2](https://doi.org/10.1175/1520-0469(2001)058<2128:sbiash>2.0.co;2)
- Corbosiero, K. L., & Molinari, J. (2002). The effects of vertical wind shear on the distribution of convection in tropical cyclones. *Monthly Weather Review*, 130, 2110–2123. [https://doi.org/10.1175/1520-0493\(2002\)130<2110:teovws>2.0.co;2](https://doi.org/10.1175/1520-0493(2002)130<2110:teovws>2.0.co;2)
- Corbosiero, K. L., & Molinari, J. (2003). The relationship between storm motion, vertical wind shear, and convective asymmetries in tropical cyclones. *Journal of the Atmospheric Sciences*, 60, 366–376. [https://doi.org/10.1175/1520-0469\(2003\)060<0366:trbsmv>2.0.co;2](https://doi.org/10.1175/1520-0469(2003)060<0366:trbsmv>2.0.co;2)
- Corbosiero, K. L., Molinari, J., Aiyyer, A. R., & Black, M. L. (2006). The structure and evolution of Hurricane Elena (1985). Part II: Convective asymmetries and evidence for vortex Rossby waves. *Monthly Weather Review*, 134, 3073–3091. <https://doi.org/10.1175/MWR3250.1>
- Dai, Y., Majumdar, S. J., & Nolan, D. S. (2019). The outflow-rainband relationship induced by environmental flow around tropical cyclones. *Journal of the Atmospheric Sciences*, 76, 1845–1863. <https://doi.org/10.1175/JAS-D-18-0208.1>
- Davis, C., Snyder, C., & Didlake, A. C. (2008). A vortex-based perspective of eastern Pacific tropical cyclone formation. *Monthly Weather Review*, 136, 2461–2477. <https://doi.org/10.1175/2007MWR2317.1>
- Didlake, A. C., & Houze, R. A. (2009). Convective-scale downdrafts in the principal rainband of Hurricane Katrina (2005). *Monthly Weather Review*, 137, 3269–3293. <https://doi.org/10.1175/2009MWR2827.1>
- Didlake, A. C., & Houze, R. A. (2013a). Convective-scale variations in the inner-core rainbands of a tropical cyclone. *Journal of the Atmospheric Sciences*, 70, 504–523. <https://doi.org/10.1175/JAS-D-12-0134.1>
- Didlake, A. C., & Houze, R. A. (2013b). Dynamics of the stratiform sector of a tropical cyclone rainband. *Journal of the Atmospheric Sciences*, 70, 1891–1911. <https://doi.org/10.1175/JAS-D-12-0245.1>
- Didlake, A. C., Reasor, P. D., Rogers, R. F., & Lee, W. C. (2018). Dynamics of the transition from spiral rainbands to a secondary eyewall in Hurricane Earl (2010). *Journal of the Atmospheric Sciences*, 75, 2909–2929. <https://doi.org/10.1175/JAS-D-17-0348.1>
- Fischer, M. S., Rogers, R. F., & Reasor, P. D. (2020). The rapid intensification and eyewall replacement cycles of Hurricane Irma (2017). *Monthly Weather Review*, 148, 981–1004. <https://doi.org/10.1175/MWR-D-19-0185.1>
- Frank, W. M., & Ritchie, E. A. (1999). Effects of environmental flow upon tropical cyclone structure. *Monthly Weather Review*, 127, 2044–2061. [https://doi.org/10.1175/1520-0493\(1999\)127<2044:eofut>2.0.co;2](https://doi.org/10.1175/1520-0493(1999)127<2044:eofut>2.0.co;2)
- Frank, W. M., & Ritchie, E. A. (2001). Effects of vertical wind shear on the intensity and structure of numerically simulated hurricanes. *Monthly Weather Review*, 129, 2249–2269. [https://doi.org/10.1175/1520-0493\(2001\)129<2249:eovwso>2.0.co;2](https://doi.org/10.1175/1520-0493(2001)129<2249:eovwso>2.0.co;2)

- Franklin, C. N., Holland, G. J., & May, P. T. (2006). Mechanisms for the generation of mesoscale vorticity features in tropical cyclone rainbands. *Monthly Weather Review*, *134*, 2649–2669. <https://doi.org/10.1175/MWR3222.1>
- Gamache, J. F. (1997). *Evaluation of a fully three-dimensional variational Doppler analysis technique*. Preprints, 28th Conference on Radar Meteorology, Austin, TX, American Meteorological Society (pp. 422–423).
- Gao, J., Xue, M., Shapiro, A., & Droegemeier, K. K. (1999). A variational method for the analysis of three-dimensional wind fields from two Doppler radars. *Monthly Weather Review*, *127*, 2128–2142. [https://doi.org/10.1175/1520-0493\(1999\)127<2128:avmfta>2.0.co;2](https://doi.org/10.1175/1520-0493(1999)127<2128:avmfta>2.0.co;2)
- Guimond, S. R., Reasor, P. D., Heymsfield, G. M., & McLinden, M. M. (2020). The dynamics of vortex Rossby waves and secondary eyewall development in Hurricane Matthew (2016): New insights from radar measurements. *Journal of the Atmospheric Sciences*, *77*(7), 2349–2374. <https://doi.org/10.1175/JAS-D-19-0284.1>
- Hence, D. A., & Houze, R. A. (2008). Kinematic structure of convective-scale elements in the rainbands of Hurricanes Katrina and Rita (2005). *Journal of Geophysical Research: Atmospheres*, *113*, 1–20. <https://doi.org/10.1029/2007JD009429>
- Hence, D. A., & Houze, R. A. (2012a). Vertical structure of tropical cyclone rainbands as seen by the TRMM Precipitation Radar. *Journal of the Atmospheric Sciences*, *69*(9), 2644–2661. <https://doi.org/10.1175/JAS-D-11-0323.1>
- Hence, D. A., & Houze, R. A. (2012b). Vertical structure of tropical cyclones with concentric eyewalls as seen by the TRMM Precipitation Radar. *Journal of the Atmospheric Sciences*, *69*, 1021–1036. <https://doi.org/10.1175/JAS-D-11-0119.1>
- Hill, K. A., & Lackmann, G. M. (2009). Influence of environmental humidity on tropical cyclone size. *Monthly Weather Review*, *137*, 3294–3315. <https://doi.org/10.1175/2009MWR2679.1>
- Jones, S. C. (1995). The evolution of vortices in vertical shear. I: Initially barotropic vortices. *Quarterly Journal of the Royal Meteorological Society*, *121*, 821–851. <https://doi.org/10.1002/qj.49712152406>
- Jorgensen, D. P., Zipser, E. J., & LeMone, M. A. (1985). Vertical motions in intense hurricanes. *Journal of the Atmospheric Sciences*, *42*, 839–856. [https://doi.org/10.1175/1520-0469\(1985\)042<0839:vmiih>2.0.co;2](https://doi.org/10.1175/1520-0469(1985)042<0839:vmiih>2.0.co;2)
- Kanamitsu, B. Y. M., Ebisuzaki, W., Jack, W., Yang, S., Hnilo, J. J., Fiorino, M., & Potter, G. L. (2002). NCEP-DOE AMIP-II Reanalysis (R-2). *Bulletin of the American Meteorological Society*, *83*, 1631–1644. <https://doi.org/10.1175/BAMS-83-11-1631>
- Keper, J. D. (2018). The boundary layer dynamics of tropical cyclone rainbands. *Journal of the Atmospheric Sciences*, *75*, 3777–3795. <https://doi.org/10.1175/JAS-D-18-0133.1>
- Landsea, C. W., & Franklin, J. L. (2013). Atlantic hurricane database uncertainty and presentation of a new database format. *Monthly Weather Review*, *141*, 3576–3592. <https://doi.org/10.1175/MWR-D-12-00254.1>
- Li, Q., & Dai, Y. (2020). Revisiting azimuthally asymmetric moist instability in the outer core of sheared tropical cyclones. *Monthly Weather Review*, *148*, 1297–1319. <https://doi.org/10.1175/MWR-D-19-0004.1>
- Li, Q., & Fang, Q. (2019). Buoyancy of convective-scale updrafts in the outer cores of sheared tropical cyclones. *Atmospheric and Oceanic Science Letters*, *12*, 58–65. <https://doi.org/10.1080/16742834.2019.1548883>
- Li, Q., & Wang, Y. (2012a). A comparison of inner and outer spiral rainbands in a numerically simulated tropical cyclone. *Monthly Weather Review*, *140*, 2782–2805. <https://doi.org/10.1175/MWR-D-11-00237.1>
- Li, Q., & Wang, Y. (2012b). Formation and quasi-periodic behavior of outer spiral rainbands in a numerically simulated tropical cyclone. *Journal of the Atmospheric Sciences*, *69*, 997–1020. <https://doi.org/10.1175/2011JAS3690.1>
- Li, Q., Wang, Y., & Duan, Y. (2017). A numerical study of outer rainband formation in a sheared tropical cyclone. *Journal of the Atmospheric Sciences*, *74*, 203–227. <https://doi.org/10.1175/JAS-D-16-0123.1>
- Lorsolo, S., Gamache, J., & Aksoy, A. (2013). Evaluation of the hurricane research division Doppler radar analysis software using synthetic data. *Journal of Atmospheric and Oceanic Technology*, *30*, 1055–1071. <https://doi.org/10.1175/JTECH-D-12-00161.1>
- May, P. T. (1996). The organization of convection in the rainbands of Tropical Cyclone Laurence. *Monthly Weather Review*, *124*, 807–815. [https://doi.org/10.1175/1520-0493\(1996\)124<0807:toocit>2.0.co;2](https://doi.org/10.1175/1520-0493(1996)124<0807:toocit>2.0.co;2)
- May, P. T., & Holland, G. J. (1999). The role of potential vorticity generation in tropical cyclone rainbands. *Journal of the Atmospheric Sciences*, *56*, 1224–1228. [https://doi.org/10.1175/1520-0469\(1999\)056<1224:tropvg>2.0.co;2](https://doi.org/10.1175/1520-0469(1999)056<1224:tropvg>2.0.co;2)
- Molinari, J., Romps, D. M., Vollaro, D., & Nguyen, L. (2012). CAPE in tropical cyclones. *Journal of the Atmospheric Sciences*, *69*, 2452–2463. <https://doi.org/10.1175/JAS-D-11-0254.1>
- Montgomery, M. T., & Kallenbach, R. J. (1997). A theory for vortex Rossby-waves and its application to spiral bands and intensity changes in hurricanes. *Quarterly Journal of the Royal Meteorological Society*, *123*, 435–465. <https://doi.org/10.1002/qj.49712353810>
- Moon, Y., & Nolan, D. S. (2015). Spiral rainbands in a numerical simulation of Hurricane Bill (2009). Part I: Structures and comparisons to observations. *Journal of the Atmospheric Sciences*, *72*, 164–190. <https://doi.org/10.1175/JAS-D-14-0058.1>
- Powell, M. D. (1990a). Boundary layer structure and dynamics in outer hurricane rainbands. Part I: Mesoscale rainfall and kinematic structure. *Monthly Weather Review*, *118*, 891–917. [https://doi.org/10.1175/1520-0493\(1990\)118<0891:blsadi>2.0.co;2](https://doi.org/10.1175/1520-0493(1990)118<0891:blsadi>2.0.co;2)
- Powell, M. D. (1990b). Boundary layer structure and dynamics in outer rainbands. Part II: Downdraft modification and mixed layer recovery. *Monthly Weather Review*, *118*, 918–938. [https://doi.org/10.1175/1520-0493\(1990\)118<0918:blsadi>2.0.co;2](https://doi.org/10.1175/1520-0493(1990)118<0918:blsadi>2.0.co;2)
- Qiu, X., & Tan, Z.-M. (2013). The roles of asymmetric inflow forcing induced by outer rainbands in tropical cyclone secondary eyewall formation. *Journal of the Atmospheric Sciences*, *70*, 953–974. <https://doi.org/10.1175/jas-d-12-084.1>
- Reasor, P. D., Eastin, M. D., & Gamache, J. F. (2009). Rapidly intensifying Hurricane Guillermo (1997). Part I: Low-wavenumber structure and evolution. *Monthly Weather Review*, *137*, 603–631. <https://doi.org/10.1175/2008MWR2487.1>
- Reasor, P. D., Rogers, R., & Lorsolo, S. (2013). Environmental flow impacts on tropical cyclone structure diagnosed from airborne Doppler radar composites. *Monthly Weather Review*, *141*, 2949–2969. <https://doi.org/10.1175/MWR-D-12-00334.1>
- Riemer, M. (2016). Meso- β -scale environment for the stationary band complex of vertically sheared tropical cyclones. *Quarterly Journal of the Royal Meteorological Society*, *142*, 2442–2451. <https://doi.org/10.1002/qj.2837>
- Riemer, M., & Montgomery, M. T. (2011). Simple kinematic models for the environmental interaction of tropical cyclones in vertical wind shear. *Atmospheric Chemistry and Physics*, *11*, 9395–9414. <https://doi.org/10.5194/acp-11-9395-2011>
- Riemer, M., Montgomery, M. T., & Nicholls, M. E. (2010). A new paradigm for intensity modification of tropical cyclones: Thermodynamic impact of vertical wind shear on the inflow layer. *Atmospheric Chemistry and Physics*, *10*, 3163–3188. <https://doi.org/10.5194/acp-10-3163-2010>
- Rogers, R., Chen, S., Tenerelli, J., & Willoughby, H. (2003). A numerical study of the impact of vertical shear on the distribution of rainfall in Hurricane Bonnie (1998). *Monthly Weather Review*, *131*, 1577–1599. <https://doi.org/10.1175/2546.1>
- Rogers, R., Lorsolo, S., Reasor, P., Gamache, J., & Marks, F. (2012). Multiscale analysis of tropical cyclone kinematic structure from airborne Doppler radar composites. *Monthly Weather Review*, *140*, 77–99. <https://doi.org/10.1175/MWR-D-10-05075.1>
- Rogers, R., Reasor, P., & Lorsolo, S. (2013). Airborne Doppler observations of the inner-core structural differences between intensifying and steady-state tropical cyclones. *Monthly Weather Review*, *141*, 2970–2991. <https://doi.org/10.1175/MWR-D-12-00357.1>

- Rozoff, C. M., Nolan, D. S., Kossin, J. P., Zhang, F., & Fang, J. (2012). The roles of an expanding wind field and inertial stability in tropical cyclone secondary eyewall formation. *Journal of the Atmospheric Sciences*, *69*, 2621–2643. <https://doi.org/10.1175/JAS-D-11-0326.1>
- Rozoff, C. M., Schubert, W. H., McNoldy, B. D., & Kossin, J. P. (2006). Rapid filamentation zones in intense tropical cyclones. *Journal of the Atmospheric Sciences*, *63*, 325–340. <https://doi.org/10.1175/JAS3595.1>
- Ryan, B. F., Barnes, G. M., & Zipser, E. J. (1992). A wide rainband in a developing tropical cyclone. *Monthly Weather Review*, *120*, 431–447. [https://doi.org/10.1175/1520-0493\(1992\)120<0431:awriad>2.0.co;2](https://doi.org/10.1175/1520-0493(1992)120<0431:awriad>2.0.co;2)
- Samsury, C. E., & Zipser, E. J. (1995). Secondary wind maxima in hurricanes: Airflow and relationship to rainbands. *Monthly Weather Review*, *123*, 3502–3517. [https://doi.org/10.1175/1520-0493\(1995\)123<3502:swmiha>2.0.co;2](https://doi.org/10.1175/1520-0493(1995)123<3502:swmiha>2.0.co;2)
- Sawada, M., & Iwasaki, T. (2010a). Impacts of evaporation from raindrops on tropical cyclones. Part I: Evolution and axisymmetric structure. *Journal of the Atmospheric Sciences*, *67*, 71–83. <https://doi.org/10.1175/2009JAS3040.1>
- Sawada, M., & Iwasaki, T. (2010b). Impacts of evaporation from raindrops on tropical cyclones. Part II: Features of rainbands and asymmetric structure. *Journal of the Atmospheric Sciences*, *67*, 84–96. <https://doi.org/10.1175/2009JAS3195.1>
- Simard, R., & L'ecuyer, P. (2011). Computing the two-sided Kolmogorov-Smirnov distribution. *Journal of Statistical Software*, *39*, 1–18. <https://doi.org/10.18637/jss.v039.i11>
- Smith, R. K., Montgomery, M. T., & Sang, N. V. (2009). Tropical cyclone spin-up revisited. *Quarterly Journal of the Royal Meteorological Society*, *135*, 1321–1335. <https://doi.org/10.1002/qj.428>
- Steiner, M., Jr, H. R. A., & Yuter, S. E. (1995). Climatological characterization of three-dimensional storm structure from operational radar and rain gauge data. *Journal of Applied Meteorology*, *34*, 1978–2007. [https://doi.org/10.1175/1520-0450\(1995\)034<1978:ccotds>2.0.co;2](https://doi.org/10.1175/1520-0450(1995)034<1978:ccotds>2.0.co;2)
- Tang, X., Lee, W. C., & Bell, M. (2014). A squall-line-like principal rainband in Typhoon Hagupit (2008) observed by airborne Doppler radar. *Journal of the Atmospheric Sciences*, *71*, 2733–2746. <https://doi.org/10.1175/JAS-D-13-0307.1>
- Tang, X., Lee, W. C., & Bell, M. (2018). Subrainband structure and dynamic characteristics in the principal rainband of Typhoon Hagupit (2008). *Monthly Weather Review*, *146*, 157–173. <https://doi.org/10.1175/MWR-D-17-0178.1>
- Terwey, W. D., & Rozoff, C. M. (2014). Objective convective updraft identification and tracking: Part I. Structure and thermodynamics of convection in the rainband regions of two hurricane simulations. *Journal of Geophysical Research: Atmospheres*, *119*, 6196–6206. <https://doi.org/10.1002/2013jd020904>
- Wadler, J. B., Rogers, R. F., & Reasor, P. D. (2018). The relationship between spatial variations in the structure of convective bursts and tropical cyclone intensification as determined by airborne Doppler radar. *Monthly Weather Review*, *146*, 761–780. <https://doi.org/10.1175/MWR-D-17-0213.1>
- Wang, Y. (2002). Vortex Rossby waves in a numerically simulated tropical cyclone. Part II: The role in tropical cyclone structure and intensity changes. *Journal of the Atmospheric Sciences*, *59*, 1239–1262. [https://doi.org/10.1175/1520-0469\(2002\)059<1239:vrwian>2.0.co;2](https://doi.org/10.1175/1520-0469(2002)059<1239:vrwian>2.0.co;2)
- Wang, Y. (2009). How do outer spiral rainbands affect tropical cyclone structure and intensity? *Journal of the Atmospheric Sciences*, *66*, 1250–1273. <https://doi.org/10.1175/2008JAS2737.1>
- Willoughby, H. E., & Chelmow, M. B. (1982). Objective determination of hurricane tracks from aircraft observations. *Monthly Weather Review*, *110*, 1298–1305. [https://doi.org/10.1175/1520-0493\(1982\)110<1298:odohtf>2.0.co;2](https://doi.org/10.1175/1520-0493(1982)110<1298:odohtf>2.0.co;2)
- Willoughby, H. E., Clos, J. A., & Shoreibah, M. G. (1982). Concentric eye walls, secondary wind maxima, and the evolution of the hurricane vortex. *Journal of the Atmospheric Sciences*, *39*, 395–411. [https://doi.org/10.1175/1520-0469\(1982\)039<0395:cwswm>2.0.co;2](https://doi.org/10.1175/1520-0469(1982)039<0395:cwswm>2.0.co;2)
- Willoughby, H. E., Marks, F. D., & Feinberg, R. H. (1984). Stationary and moving convective bands in hurricanes. *Journal of the Atmospheric Sciences*, *41*, 3189–3211. [https://doi.org/10.1175/1520-0469\(1984\)041<3189:samcbs>2.0.co;2](https://doi.org/10.1175/1520-0469(1984)041<3189:samcbs>2.0.co;2)
- Wingo, M. T., & Cecil, D. J. (2010). Effects of vertical wind shear on tropical cyclone precipitation. *Monthly Weather Review*, *138*, 645–662. <https://doi.org/10.1175/2009MWR2921.1>
- Yu, C. K., & Chen, Y. (2011). Surface fluctuations associated with tropical cyclone rainbands observed near Taiwan during 2000–08. *Journal of the Atmospheric Sciences*, *68*, 1568–1585. <https://doi.org/10.1175/2011JAS3725.1>
- Yu, C. L., & Didlake, A. C. (2019). Impact of stratiform rainband heating on the tropical cyclone wind field in idealized simulations. *Journal of the Atmospheric Sciences*, *76*, 2443–2462. <https://doi.org/10.1175/JAS-D-18-0335.1>
- Yu, C. L., Didlake, A. C., Zhang, F., & Nystrom, R. G. (2021). Asymmetric rainband processes leading to secondary eyewall formation in a model simulation of Hurricane Matthew (2016). *Journal of the Atmospheric Sciences*, *78*, 29–49. <https://doi.org/10.1175/JAS-D-20-0061.1>
- Yu, C. K., Lin, C. Y., Cheng, L. W., Luo, J. S., Wu, C. C., & Chen, Y. (2018). The degree of prevalence of similarity between outer tropical cyclone rainbands and squall lines. *Scientific Reports*, *8*, 1–15. <https://doi.org/10.1038/s41598-018-26553-8>
- Yu, C. K., & Tsai, C. L. (2013). Structural and surface features of arc-shaped radar echoes along an outer tropical cyclone rainband. *Journal of the Atmospheric Sciences*, *70*, 56–72. <https://doi.org/10.1175/JAS-D-12-090.1>
- Zhang, J. A., Rogers, R. F., Reasor, P. D., Uhlhorn, E. W., & Marks, F. D. (2013). Asymmetric hurricane boundary layer structure from dropsonde composites in relation to the environmental vertical wind shear. *Monthly Weather Review*, *141*, 3968–3984. <https://doi.org/10.1175/MWR-D-12-00335.1>